

Adaptive Mesh Modelling of the Thermally Driven Annulus

DPhil Second Year Report

J. R. Maddison

Atmospheric, Oceanic and Planetary Physics

University of Oxford

maddison@atm.ox.ac.uk

Supervisors:

Prof. P. L. Read, Prof. D. P. Marshall, Dr. M. D. Piggott

August 31, 2009

Abstract

The rotating annulus is a classic laboratory scale analogue for geophysical fluid flows. There have been over five decades of research into annulus systems, in a broad range of regimes and altered geometries. Some annulus regimes contain dynamics on multiple scales, posing challenges for traditional fixed mesh simulations. Others have complicated physical boundaries, which are difficult to represent in a satisfactory manner using traditional structured meshes. This report details the first two years of DPhil work in which the in-development Imperial College Ocean Model (ICOM) is applied to simulations of the thermally driven annulus. ICOM implements new technologies, including the use of fully unstructured meshes and dynamic mesh adaptivity techniques. Hence ICOM simulations can allow meshes to conform to system boundaries, and also to adapt to the dynamics of the flow as they evolve. Previous annulus research allows ICOM to be validated against a well-studied, carefully controlled laboratory system. In addition to this, the technologies under development in ICOM present an opportunity to simulate the annulus in previously challenging regimes and geometries.

In this report, ICOM is applied to the classic heat flow rotating annulus and compared against existing laboratory data. It is shown that the model is able to reproduce key features of the flow. It is further shown that the introduction of dynamic mesh adaptivity influences the resulting solution in unexpected ways. The application of fully unstructured dynamic mesh adaptivity to simulations of geophysical fluids is discussed, with emphasis on open questions that are introduced when transferring techniques from computational fluid dynamics.

Using knowledge of the strengths (and weaknesses) of ICOM technologies derived from comparisons with the heat flow annulus, ICOM is further applied to simulations of non-standard and traditionally difficult to simulate annulus geometries. These focus on full radial barrier annulus simulations. Some numerical results for these configurations are presented, compared with previous work, and used to investigate the physics of the system.

Contents

1	Introduction	3
1.1	The Annulus	4
1.2	ICOM / Fluidity	4
1.3	Projection Description	5
1.4	Summary	6
2	The Thermally Driven Annulus	7
2.1	Motivation: The Annulus as a Laboratory Scale Analogue	7
2.2	Sloping Convection	10
2.3	Annulus Regimes	12
2.4	Previous Work	13
2.5	Summary	15
3	The Imperial College Ocean Model	16
3.1	Unstructured Finite Element Methods	16
3.2	Balance Considerations	19
3.3	Mesh Adaptivity	23
3.4	Summary	26
4	Model Validation	28

<i>CONTENTS</i>	2
4.1 Verification versus Validation	28
4.2 Heat Transport Validation	29
4.3 Static Structured Mesh Simulations	31
4.4 Adaptive Mesh Simulations	33
4.5 Mesh Adaptivity Errors	35
4.6 Mesh Projections	38
4.7 Balance Considerations	40
4.8 Summary	41
5 The Radial Barrier Annulus	43
5.1 Topological Effects	43
5.2 ICOM Simulations of the Radially Blocked Annulus	45
5.3 Heat Transport	46
5.4 Summary	50
6 Summary and Future Work	51
6.1 Future Work	51
6.2 Timeline for Completion	53
6.3 Summary	53
A Equations of Fluid Flow	55
B Dimensionless Parameters	57

Chapter 1

Introduction

In the investigation of any physical system there is a competition between the observations that are required in order to test hypotheses, and the impacts of those observations on the system under investigation. It is fundamental to scientific investigation that any measured value has an inherent error introduced by the very act of measurement. This can make direct observations of characteristics of a system difficult, leading to more indirect or incomplete observations and with an impact on the resulting conclusions that can be drawn. Worse, many physical systems, particularly those in geophysical fluid dynamics, are difficult if not impossible to measure directly at all. It may not always be practical or technologically possible to take direct measurements of the interiors of objects such as the Jovian planets, or not be possible to force a system such as a rotating fluid tank into conditions of interest, such as for very fast or very slow rates of rotation.

Instead of investigating the system directly, there is much to be gained by taking one step back and developing a model of the system to be investigated. Theoretical models are built upon assumptions, often chosen through necessity in order for the theories to be tractable, but even where this is the case these assumptions give an insight into which physical features are essential and which can safely be neglected without significant loss of behaviour [Lorentz, 1967]. Indeed, it is often failures of theories and the resulting necessary relaxation of assumptions that leads to insight into new physics.

In a not unrelated manner, laboratory models can be constructed to represent a system that is difficult to control or measure directly. While it is clearly impossible to capture the full range of atmospheric dynamics in a table-top experiment, it is possible nevertheless to create a system including just those features necessary in order to investigate an essential subset of those dynamics [Hide, 1969, Hide and Mason, 1975]. These laboratory models can then be made progressively more complex in order to introduce new features present in the larger modelled system.

While laboratory experiments can go some way to filling gaps in understanding, they can themselves be limited by technological capabilities or the influence of measurements on the experiment. This DPhil concerns the investigation of underlying physics of geophysical fluid dynamics. Hence, while there is undoubtedly much to be gained from direct modelling via general circulation models, this DPhil instead focuses on numerical models of laboratory analogues. Numerical models can be used to explore otherwise inaccessible physical regimes, and can diagnose physical quantities without the resulting impact of measurement on the system under observation. Complementary to this, the focus on laboratory scale analogues filters out many of the features of atmospheric dynamics, enabling the essential processes to be studied while simultaneously enabling direct comparison between numerical model and experiment, ensuring that the model is a realistic representation of the physical world.

1.1 The Annulus

The annulus is a classic laboratory scale analogue used to allow the investigation of geophysical fluid dynamics under controllable and reproducible conditions. Two of the key factors driving the physics of atmospheres, the influence of rotation and differential heating and cooling [Fultz, 1951], are introduced in the annulus via rotation of the system about its axis of symmetry and through differential heating and cooling of the tank inner and outer cylindrical side-walls.

This “base” configuration can be extended depending on the physics of interest to be studied, through variations in forcing and in geometric or topological characteristics. These experiments have given an extremely detailed picture of the rotating annulus, allowing much of the physics of the system to be explained and hence gaining an insight into geophysical fluid dynamics as a whole. However, the inherent issues with experiment persist. The dynamics of the annulus can be, depending on the experimental details, highly non-linear, and may be sensitive to intrusive measurement techniques or imprecise experimental control. A commonly encountered example is the use of in-situ thermocouple measurements, which have been cited as possible causes for inconsistencies between individual experiments [James et al., 1981], and for inconsistencies between experiment and numerical models [Hignett et al., 1985, Young and Read, 2008a]. Additionally, experiments are limited by what can be physically constructed. Hence there are significant potential benefits from numerical simulations of the rotating annulus, in addition to and along side laboratory experiments.

1.2 ICOM / Fluidity

The Imperial College Ocean Model (ICOM) is a next-generation ocean model being developed by Imperial College London and its collaborators (including the University of Oxford). ICOM is an application of the general-purpose com-

putational fluidity dynamics (CFD) framework Fluidity; ICOM simulations are Fluidity run with a particular set of “ocean mode” model parameters. Fluidity itself is being applied to an extremely wide range of fluid flows, for both physical and engineering applications. Fluidity includes a range of cutting-edge numerical techniques, most of which are available for use in ocean-mode ICOM simulations.

ICOM is, and has been for the duration of this DPhil project, under heavy and continual development. While this is advantageous, in that new features are implemented regularly or coding errors are eradicated, it also has a negative impact on simulation reproducibility and is a source of model instability. This, combined with the unusually long run-time of ICOM simulations (see chapter 3 for details), acts as an impediment to applied research using ICOM. Several essential model features have been sufficiently poorly documented, maintained, or tested, that their use for this project has required their full re-implementation (details of a new model interface are described in Ham et al. [2008]). In addition to this, the model is generally lacking diagnostic tools. The use of general unstructured meshes by the model (described in section 3.1) makes the creation of new diagnostics technically challenging and time consuming when compared to structured mesh equivalents. Work to be detailed in the remainder of this report has been significantly impacted by these issues.

1.3 Projection Description

There are two key motivations for this DPhil project:

1. The advanced numerical techniques implemented and under development in Fluidity present an opportunity to simulate annulus regimes and geometries that, due to technical difficulties with existing models, it has previously proven challenging or impossible to simulate.
2. Fluidity has proven applications in a CFD context, but many of the numerical methods it implements are untested in a geophysical context. The wealth of previous experimental annulus research, combined with its relative simplicity (compared to full global ocean modelling), make it an ideal system for the purposes of validation of ICOM as a geophysical fluid dynamics model.

Hence the key aims of this project are to:

1. Use the annulus as a validation test case for the purposes of assessing the applicability (or otherwise) of ICOM technologies in a geophysical context.
2. Based on this assessment, to use applicable technologies for the purposes of investigating the physics of the rotating annulus in previously inaccessible regimes and geometries.

1.4 Summary

The format of this report will be as follows: Chapter 2 will give a brief introduction to the physics of the rotating annulus, from the early experiments through to the more modern investigations into the higher order dynamics of the system. It will go on to present key open questions that remain in understanding the physics of the rotating annulus, with emphasis on those questions that have the potential to be addressed through numerical modelling. Chapter 3 will discuss ICOM, listing the technologies that present new opportunities for simulations of the rotating annulus. Chapter 4 will discuss a validation exercise conducted using the rotating annulus as a test case, and questions that have arisen from this validation. Chapter 5 will go on to discuss simulations of a previously challenging annulus configuration: simulations of the annulus with a full radial barrier. The report will conclude in chapter 6 with an outline of work to be conducted in order to complete this DPhil project, together with a timetable for project completion.

Chapter 2

The Thermally Driven Annulus

The rotating annulus is a classic laboratory scale analogue for geophysical flows with over a half a century of research already conducted. In this chapter an overview of the justifications for the use of annulus experiments as an analogue for geophysical flows will be given. A key feature of annulus dynamics, baroclinic instability, will be described, and an overview of observed flow behaviours will be supplied. To conclude, a summary of more recent research conducted in this field will be given, together with a summary of key avenues that are open for numerical research.

2.1 Motivation: The Annulus as a Laboratory Scale Analogue

There have been efforts to capture the physics of global atmospheric dynamics on small scales since the mid 19th century. The goals of these experiments, to quote Lorentz [1967] “*consist of suppressing certain supposedly irrelevant details so that the important processes may be more readily examined*”¹. Hence while atmospheric dynamics are undoubtedly complex, they contain distinct layers of complexity and may, largely, be driven by a small number of underlying principles.

Early attempts to produce such analogues were conducted by Vettin [1857]. These experiments, an example of which is shown in figure 2.1, initially used point-wise heating on a rotating disc of air. Later experiments used ice at the disc centre, giving a more atmospheric-like thermal forcing and constituting

¹This exact quote is in a discussion of theoretical models, although the scope can be extended as it is stated in the context of laboratory models

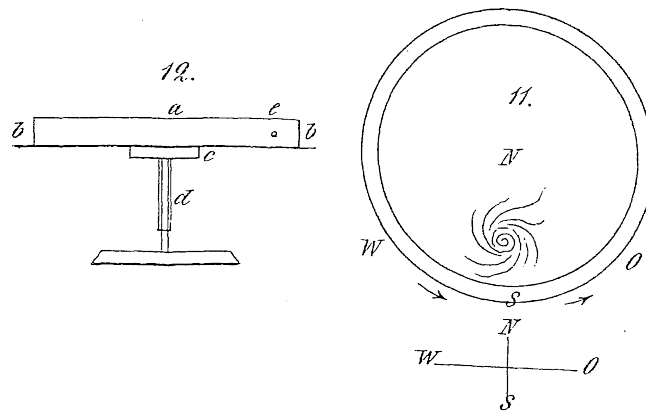


Figure 2.1: A rotating air disk experiment, from Vettin [1857]. A cardboard disk with glass base and lid is rotated, and heated from below at a single point. Smoke is blown into the disk (point “e” left) as a passive tracer. The heating produces a convective cyclone [Fultz et al., 1959].

an early “dishpan” type laboratory analogue for atmospheric dynamics [Fultz, 1951, Fultz et al., 1959]. The dishpan laboratory analogue is a logical first step in the construction of a laboratory model for the atmosphere, but it suffers from setbacks in terms of interpretation - in particular it lacks reproducibility.

In 1950 Raymond Hide, while studying for a PhD in geodesy, applied a similar principle to the research of motion of the Earth’s outer core, postulating that a differentially heated rotating annulus could prove a useful analogue for this. This annulus system was constructed using spare materials, with a configuration as shown in figure 2.2 [Hide, 1953, 2006], and can be thought of as the standard annulus configuration. On the first run of the experiment a stable wavenumber four type disturbance was observed within the annulus. This has since been recognised to be a manifestation of a dynamical shear instability known as baroclinic instability [Hide and Mason, 1975], early theories of which are described by Charney [1947] and Eady [1949]. These annulus experiments were only later recognised for their relevance to atmospheric dynamics [Hide, 2006], and for their similarities to atmospheric flows (see figure 2.3). A key advantage of these experiments was their reproducibility - this was one of the breakthroughs supporting early work on deterministic chaos [Lorenz, 1963].

More precisely, the equations governing the dynamics of a system can be re-expressed in terms of non-dimensional variables (normalisation) generating a series of dimensionless parameters expressing the scale of a system relative to system coordinates. The dynamics of two systems with matched dimensionless parameters in the non-dimensional coordinates (more precisely, the trajectory of the two systems through phase space) which have an identical initial condition (starting at the same point in phase space) and boundary conditions must necessarily be identical, and hence two such systems are said to be “dynamically

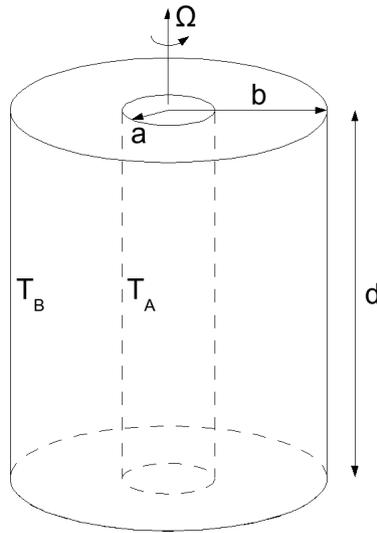


Figure 2.2: A standard thermally driven annulus configuration. The annulus is rotated about its axis of symmetry at constant rate Ω and the flow is driven by differential heating and cooling of the inner and outer side walls, which are held at temperatures T_A and T_B respectively ($T_A \neq T_B$). The upper lid may be free or in contact with a rigid boundary.

similar” [Batchelor, 1967]. Hence for an annulus configuration with a given set of external parameters there is an infinite (in each parameter) set of configurations which, in non-dimensional co-ordinates, exhibit the same behaviour. There are, for a standard free-surface annulus configuration, 30 such dimensionless parameters [Fowlis and Hide, 1965]. For a Boussinesq model with linear equation of state and rigid lid only six of these are retained: these are given in appendix B.

Beyond this standard configuration there are a series of higher order effects that can be introduced for more realistic representations of certain aspects of atmospheric dynamics. The effect of the variation of rotation influence with latitude can, to a limited extent due to fluid baroclinicity, be introduced via sloping upper and/or lower boundaries [Mason, 1975]. The effect of topography can be introduced with still more complex upper and lower boundaries [Risch, 1999] and the effect of continental boundaries on ocean dynamics can be simulated via the insertion of radial barriers [Hide, 1997, Rayer et al., 1998, Wordsworth, 2008].

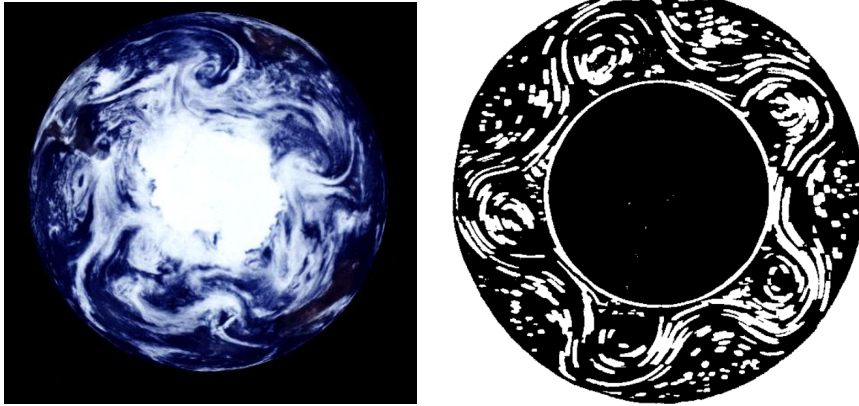


Figure 2.3: Left: A transient wavelike structure (wavenumber 4 to 5) observed in the antarctic (Galileo composite image) [NASA/JPL]. Right: A baroclinic wave observed in a thermally driven annulus (from Hide and Mason [1975], figure 4).

2.2 Sloping Convection

One of the most striking features of a typical (i.e. weakly non-linear with well-defined waves [Read, 1992]) thermally driven annulus experiment is a wave or series of wave dominating the flow, as shown in figure 2.3.

Consider a simplified 2D case: fluid in a square cavity subject to gravity and differentially heated on its side walls. Let this fluid be given an initial condition of linear temperature variation, varying from left to right. With this initial condition there is a potential energy density gradient creating a gravitational torque [Hide and Mason, 1975] and driving an overturning circulation. At large time (and for sufficiently high Rayleigh number) the flow has two distinct regions: a viscosity dominated region, in which the fluid relaxes towards a non-rotating stably stratified temperature profile with quasi-horizontal temperature contours [Read, 1992], and a diffusion dominated boundary layer region with near vertical temperature contours [Gill, 1966, Read, 1992].

Now let this geometry be extended into the third dimension to form an annular chamber. In the non-rotating case the dynamics are as in the 2D case, albeit with a small geometric modification. If the annulus is now rotated about its axis of symmetry the radial overturning circulation is inhibited by the Coriolis force - a geostrophically balanced flow cannot be supported in the radial direction, as no single valued azimuthal pressure gradient can exist to balance an azimuthal Coriolis force. This inhibits thermal transport from the outer to inner annulus side walls, leading to an increasingly diffusion dominated interior and acting to tilt interior temperature contours. Hence density isosurfaces (isopycnals - parallel to temperature contours for a fluid with a linear equation of state) become tilted away from the horizontal [Hide and Mason, 1975, Read, 1992]

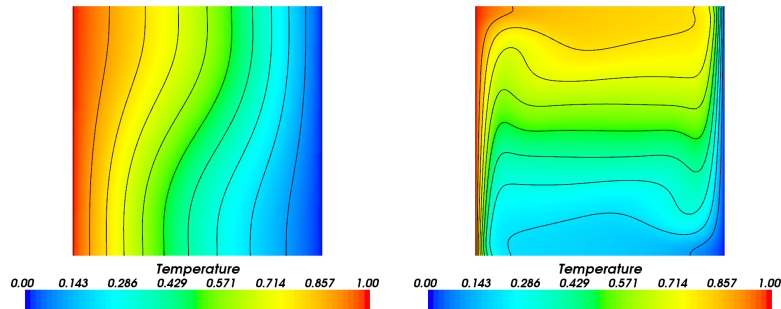


Figure 2.4: Two dimensional ICOM simulations of the natural convection in a square cavity problem for a Boussinesq Prandtl number 0.71 fluid as described by de Vahl Davis and Jones [1983]. Left: At Rayleigh number 10^3 the thermal boundary layers have thickness ~ 0.2 [Gill, 1966, MORALS] and the dynamics are largely diffusion dominated. Right: At Rayleigh number 10^6 the thermal boundary layers have thickness $0.03/L$ [Gill, 1966, MORALS] and there is an extensive advection dominated inner region [Read, 1992, Donea and Huerta, 2003]. 10 temperature contours shown. Typical annulus Rayleigh numbers are $\sim 10^7$, putting it well in the advection dominated regime.

creating a definitively baroclinic fluid [Vallis, 2006]. Hence there is a region of instability (as shown in figure 2.5) within which there is an opportunity for, in parcel exchange across isopycnals, potential energy release. In the rotating thermally driven annulus the flow is conditionally unstable against “sloping” convection, with the instability gaining energy via the extraction of potential energy of the system.

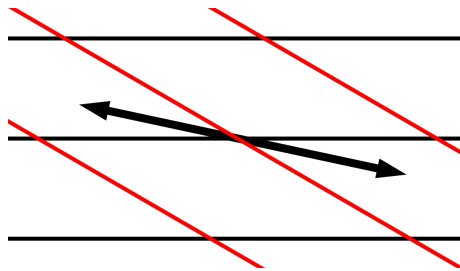


Figure 2.5: Sloping convection - geopotential contours in black, isopycnals in red [Hide and Mason, 1975]. In fluid parcel exchanges between the regions indicated there is a net potential energy release.

Note that the presence of baroclinicity is in no sense a sufficient requirement for sloping convection to actually occur - it is merely a superficial explanation of the energetics of the instability. It fails to take into account conservation principles, in particular conservation of potential vorticity. The conservation principles can be built into more mathematical analyses, often conducted using

quasi-geostrophic models. Two early such models for this process are described by Charney [1947] and Eady [1949], with its extension for the annulus in Hide [1969] and Hide and Mason [1975]. In particular, it should be noted that, for the annulus, the inclusion of Ekman layer boundary conditions is essential for Eady-type models to give a realistic description of the instability region [Barcilon, 1964, Hide, 1969] - the Ekman layers are “active” boundary layers. Eady-type models themselves appear to be rather an unsatisfactory explanation of the annulus system, with many of the built-in assumptions (particularly the assumption of zero bulk potential vorticity and constant stratification) being generally poorly satisfied in the annulus. Also, the zero bulk potential vorticity assumption is an apparent violation of the Charney-Stern-Pedlosky conditions for baroclinic instability [Vallis, 2006], requiring more exotic boundary modified potential vorticity formulations in order for this contradiction to be resolved [Bretherton, 1966]. These modifications are not universally accepted as valid [Green et al., 1987]. These failings have led to attempts to generate more advanced models incorporating more realistic flow profiles [Bell and White, 1988]. However, the simple “zero potential vorticity” models provide a remarkably accurate description of mode transitions in the annulus [Hide and Mason, 1975].

2.3 Annulus Regimes

For varied choices of external parameters the annulus exhibits a number of distinct behaviours, or regimes. The broad regimes are, in order of increasing rate of rotation [Mason, 1975, Read, 1992]:

1. Axisymmetric: There are two distinct axisymmetric regimes, a super-stratified “upper-symmetrical” Hadley regime with thermal wind balance in the bulk leading to a prevailing “westerlies” flow, and a diffusion dominated “lower symmetrical” regime.
2. Weakly non-linear: The axisymmetric regime becomes unstable and baroclinic instability is observed. The linear instability is equilibrated by non-linear effects (finite amplitude equilibration).
3. Irregular: A transition to turbulent dynamics.

Within the weakly non-linear regime there are a series of wavenumber mode transitions (see figure 2.6) together with a number of observed sub-regimes corresponding to higher order instabilities. These include amplitude vacillation (periodic variation in wave amplitude) and structural vacillation (low dimensional chaotic regimes). In addition to this, solutions are not unique for a given set of external parameters - hysteresis is observed, with wavenumber transition points being a function of the direction from which they are approached in phase space [Read, 1992, Sitte and Egbers, 2000].

While there are a number of non-dimensional parameters defining the flow, annulus regimes are typically defined in terms of just two: the thermal Rossby

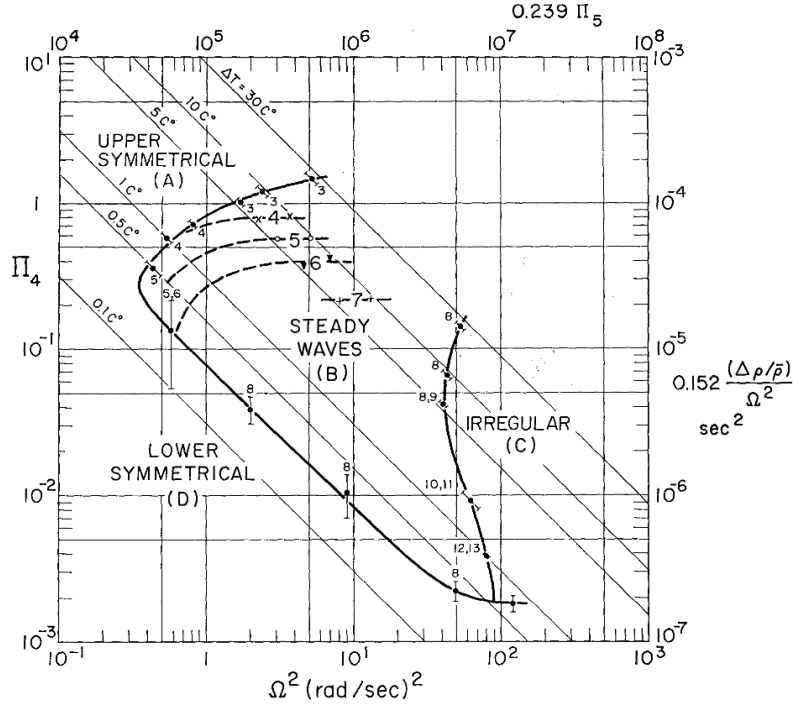


Figure 2.6: A typical annulus regime diagram for thermally driven annulus experiments (here with a free surface), from Fowles and Hide [1965] figure 3. Here $\Pi_4 = \Theta = [g\alpha\rho'd]/[(b-a)^2\Omega^2]$ is the thermal Rossby number, and $\Pi_5 = T = [4(b-a)^5\Omega^2]/[\nu^2d]$ the Taylor number (symbols as in appendix A). The diagonal full lines indicate lines of constant $(T_B - T_A)$. The full curved lines indicate centres of regime transitions, and the bars their width and wavenumber. The curved dashed lines indicate wavenumber transitions.

number (or Hide number):

$$\Theta = \frac{g\alpha(T_B - T_A)}{\Omega^2} \frac{d}{(b-a)^2}, \quad (2.1)$$

and the Taylor number:

$$T = \frac{\Omega^2 4(b-a)^5}{\nu^2 d}. \quad (2.2)$$

Here a is the minor annulus radius, b is the major annulus radius, d is the tank depth, g is the gravitational acceleration, α is the thermal expansion coefficient, ν is the kinematic viscosity, Ω is the strength of rotation and T_A and T_B are the temperatures of the inner and outer tank walls respectively. The Taylor number

is essentially a rotational Reynolds number, expressing the strength of rotation relative to viscosity [Lorentz, 1967, Hide and Mason, 1975]. It is empirically found to be the ordinate that best collapses annulus regimes onto a single regime diagram in experiment [Fowles and Hide, 1965] and is a free parameter defining the location of the regime diagram “knee” (the turning point in the anvil of instability in a regime diagram as in figure 2.6) when performing linear stability analysis for the annulus [Hide, 1969]. The thermal Rossby number defines the strength of buoyancy to rotation. Hence, combined, the Taylor number and thermal Rossby number give an indication of the two dominating features of geophysical flows [Lorentz, 1967].

2.4 Previous Work

The original annulus experiments were conducted in the PhD work of R. Hide [Hide, 1953] with a discussion of the history of the experiments in Hide [2006] and a definitive summary of the first two decades of research given in Hide and Mason [1975]. Fultz et al. [1959] details more modern dishpan experiments alongside annulus experiments. Work on the internally heated annulus is described in Hide and Mason [1970], while a study of annulus experiments with sloping boundaries is given in Mason [1975].

More recently, research into annulus experiments with radial barriers has been conducted by Rayer [1992] and Rayer et al. [1998], with particular reference to the influence of rotation on simply connected systems and the consequences for the system thermal transport. Work on finite dimensional chaos is detailed in Fruh and Read [1997] observed in a “modulated” amplitude vacillation annulus mode.

In terms of numerical simulations, early work was conducted by Williams [1969] in which the Navier-Stokes equations were solved on a regular structured mesh in cylindrical coordinates. These simulations reproduced a (quote) “*finite amplitude Eady wave*”. A somewhat more advanced model for the annulus of a similar type was developed by Farnell and Plumb [1975, 1976] using a tanh stretched mesh to concentrate computational resources in the side-wall (thermal) and lid and base (Ekman) boundary layers (an a-priori adapted mesh). These simulations were compared with experiment in James et al. [1981], where it was noted that the model gave a good representation of low wavenumber flows, while at higher wavenumbers discrepancies were attributed to limited grid resolution. Also, the wavenumber transitions points were found to not correspond exactly with experiment. Further comparison work was conducted by Hignett et al. [1985], in which the accuracy of the same finite difference model was tested over a wider range of regimes, including comparison of the system heat transport to experiment. The heat transport of the system was found to be poorly represented by the model, attributed to limitations on model resolution. Still more recently, this model has been used to investigate heat transport in the context of eddy parameterisations in Read [2003], for more detailed regime diagram tracing in Young and Read [2008a] and for work on forecasting techniques in Young and

Read [2008b]. Taking a slightly different approach, a quasi-geostrophic model for the annulus is described by Williams et al. [2009], while regime diagram tracing for an annulus-type hemispherical shell geometry using a general circulation model is described by Geisler et al. [1983].

Simulations of non-standard annulus geometries have been attempted, but are limited in scope. More general mesh representations were attempted in the DPhil work of Elliott [1995]. Here, a control volume finite element model was created, with the aim of being able to study a wide range of annulus problems, such as sloping annulus geometries. Technical issues prevented this being applied to full 3D annulus simulations. In Risch [1999] topographic simulations were conducted, initially using a modified version of the Farnell and Plumb [1975, 1976] code and (as this was found to be unsuccessful) with a modified version of an early MIT model. Both implementations suffered from boundary conforming issues. Simulations of the full radial barrier annulus were conducted using another modified version of the Farnell and Plumb [1975, 1976] code in Rayer [1992, 1994], although the model was found to a poor representation of the horizontal flow in the region of the inner tank wall.

Despite the enormous wealth of experimental data available for the annulus, there have been remarkably few numerical simulations of the system. The numerical simulations that have been conducted have generally been confined to the simplest annulus geometries, with a rigid in-contact upper boundary (so that no prognostic equation for free surface need be solved) and horizontal upper and lower boundaries. More exotic simulations such as with radial barriers or topography have been given little attention. Although this would have been possible through the work of Elliott [1995], this model has not been successfully applied to the full 3D problem. Further to this, many comparison works have cited lack of model resolution as a source of inconsistency between model and experiments. Hence unstructured mesh techniques present an opportunity to simulate more complex domains, while dynamic mesh adaptivity techniques, in which the mesh can be optimised based upon the flow dynamics, have the potential to produce simulations of increased accuracy and physical relevance.

2.5 Summary

The thermally driven annulus is a classic analogue for geophysical flows with decades of previous research. It contains a number of possible flow regimes, including laminar axisymmetric, non-linear with fully developed baroclinic waves with unstable or chaotic sub-regimes, and turbulent regimes. The large wealth of experimental data makes the thermally driven annulus an ideal test case for geophysical simulations, while at the same time there are few numerical simulations of non-standard annulus configurations.

The next chapter will describe the Imperial College Ocean Model, an ocean model currently under development with the potential to simulate the thermally driven annulus with increased detail and accuracy, and in regimes and

geometries that have not previously been studied numerically.

Chapter 3

The Imperial College Ocean Model

The Imperial College Ocean model (ICOM) is a next-generation ocean model, currently under development. It is itself an application of the more general computational fluid dynamics code Fluidity, which has a diverse range of applications in the study of fluid flows.

This chapter will describe the technologies implemented and being developed for ICOM, and will detail their potential advantages to simulations of the thermally driven annulus. The three key technologies implemented in ICOM presenting opportunities to conduct new annulus related research are that [Pain et al., 2005]:

1. ICOM uses 3D, anisotropic, unstructured meshes;
2. ICOM has techniques for accurate representation of physical balance on unstructured meshes;
3. ICOM uses dynamic mesh optimisation techniques.

Each of these technologies will now be described in turn, together with their potential benefits for simulations of the thermally driven annulus and identification of possible issues.

3.1 Unstructured Finite Element Methods

The current state-of-the-art global ocean models, as well as the Boussinesq Navier-Stokes model of Farnell and Plumb [1975, 1976] used in Hignett et al.

[1985], Read [2003] and Young and Read [2008a], are built upon structured finite difference technologies [Griffies et al., 2000]. ICOM, on the other hand, is being developed using full 3D anisotropically unstructured finite element methods.

In any numerical simulation, unstructured or otherwise, a finite dimensional computational domain must be defined, usually through a partitioning into a computational mesh¹. The defining feature of structured meshes is that there is a prescribed mesh topology with some common, usually simple, neighbourhood relationship between adjacent nodes and elements (sub-volumes) in the mesh. This has significant benefits in terms of computational efficiency, as well as implementation simplicity [Griffies et al., 2000, Chen et al., 2007]. However, these methods struggle to conform to domain boundaries that are inconsistent with the prescribed structured mesh connectivity [Chen et al., 2007], as shown in figure 3.1. This issue can, to some degree, be overcome using shaved or partial cell methods, or using more exotic space filling curve techniques such as the Sierpinski curve method of Bader et al. [2008]. However, the point is still valid that structured meshes, by their very definition, impose constraints upon the topology that they can support. As will be discussed later in section 3.3, this imposes limitations upon the application of mesh adaptivity to these methods.

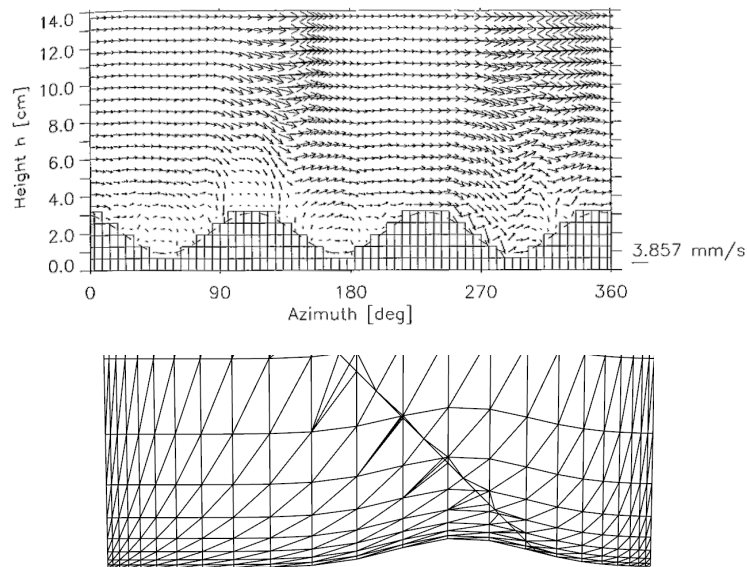


Figure 3.1: Above: A computational mesh used in simulations of the topographic annulus from Risch [1999] figure 4.5, using a modified version of the early MIT model. Note boundary staircasing. Below: A structured, non-uniform conforming mesh for simulations of the topographic annulus using ICOM. The apparent mesh complexity in the latter is caused by visualising slices through tetrahedra.

Unstructured mesh techniques, on the other hand, relax the simple neighbourhood relationship constraint on the mesh. In their most common implementa-

¹Mesh free (or “particle”) methods are a notable exception.

tion, domains are divided into simple polytopes with elements sharing adjacent faces. These can conform to an arbitrary bounding topography in a natural way. Furthermore, it is, once a general unstructured mesh implementation is in place, relatively trivial to choose a mesh that resolves internal features with either a priori or dynamic mesh adaptivity.

Finite difference techniques, while being undoubtedly at present the dominant method for large scale atmosphere and ocean models, are extremely difficult to extend to unstructured meshes. In a finite difference discretisation an approximation for the governing equations is made by replacing derivatives with differences between nodal values on the mesh. Finite element methods on the other hand (and related finite volume methods) instead define finite dimensional basis functions within each element in the mesh. These basis functions are then used to find an approximate solution to the governing equations (technically a projection of the solution field onto a discrete subspace). This has the benefit of defining a solution over the entire computation domain, but more significantly can be applied to unstructured mesh methods in an entirely natural way. Furthermore, the element basis functions used can be chosen to suit the problem simulated - for example using upwinding of the element basis functions for advective stabilisation methods, or choosing appropriate solution continuity at element boundaries with varying degrees of differentiability. This idea will be returned to in section 3.2, where it will be seen how element choice impacts balance errors in physical systems.

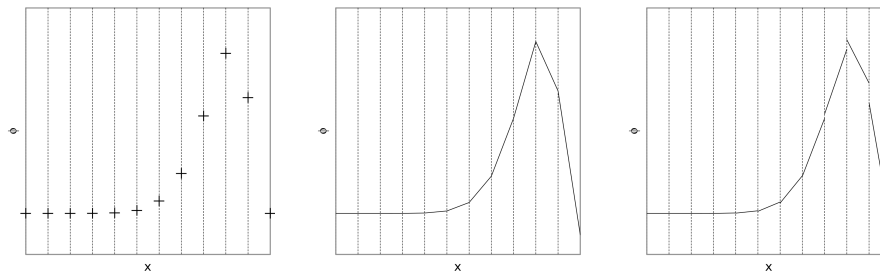


Figure 3.2: Discretisation comparison. Left: Finite difference - the solution is defined node-wise. Centre: Piecewise linear continuous finite element ($P1$). Right: Piecewise linear discontinuous finite element ($P1_D$). Note how the discontinuous method captures the sharp gradients, illustrating how element types can be chosen depending on the application.

There are three primary types of finite element discretisations implemented in Fluidity; continuous Galerkin (CG), discontinuous Galerkin (DG), and control volume (CV). In a continuous Galerkin finite element formulation a strong continuity constraint is imposed on the solution, by insisting that the solution itself must be continuous everywhere within the simulation domain. In a discontinuous Galerkin discretisation this condition is relaxed, and a weak continuity constraint is applied at element interfaces by imposing that integrated fluxes over adjoining element boundaries are equal [Donea and Huerta, 2003], but al-

lowing the solution itself to be discontinuous. DG methods necessarily have an increased number of degrees of freedom over CG methods for a given set of elements, but have been shown to give improved accuracy for a given numerical cost for certain (particularly non-smooth) applications [Sherwin, 2007]. In contrast to these, in a control volume finite element formulation differential equations are cast to integral equations concerning fluxes integrated about control volumes around nodal points (integrated over the dual mesh).

An introduction to finite element methods from the perspective of linear algebra is given in Strang [1988]. A more detailed discussion with application to flow problems is given in Zienkiewicz and Taylor [2000] and Donea and Huerta [2003]. Details of upwind stabilisation methods for CG advection problems are given in Raymond and Garder [1976], Brooks and Hughes [1982], Hughes [1987], Donea and Huerta [2003] and Ford et al. [2004a]. Detailed discussions of the control volume finite element method are given in Risch [1999], while details of flux limiters for control volume methods are given in Sweby [1984] and Leonard [1991]. The details of the discretisation of the Navier-Stokes equation and accompanying heat transport equation by Fluidity are given in Ford et al. [2004a,b] for cubic elements and in Piggott et al. [2008] for simplex elements. The exact equations solved by Fluidity are given in appendix A

The key benefits of unstructured mesh numerical methods for simulations of the thermally driven annulus are therefore: that they can conform to bounding topography in a natural way, and that they allow for the application of mesh adaptivity techniques. Finite element methods additionally define the solution fields over the entirety of the simulation domain, and not simply at node points, meaning that in principle diagnostics can be computed in a rigorous manner. Despite their potential benefits, unstructured meshes have been slow to be adopted for ocean models. While they are not uncommon for coastal [Chen et al., 2007, Bajo et al., 2008] and tidal modelling, there are key perceived difficulties with unstructured meshes. They are generally thought to suffer from problems such as wave scattering at resolution boundaries, difficulties in accurately representing physical balance [Griffies et al., 2000], as well as having significantly more complex implementations [Chen et al., 2007].

3.2 Balance Considerations

It is of vital importance that a numerical model of a geophysical fluid, such as the rotating annulus, be able to represent balance accurately. Geophysical flows, including the rotating annulus, are generally in geostrophic and hydrostatic balance to leading order. Hence any error in representation of balance can lead to a serious pollution of numerical solutions. It has been observed that unstructured mesh simulations of systems that are close to physical balance suffer from an additional numerical instability, whose nature is similar to the pressure gradient errors of sigma coordinate models [Haney, 1991, Ford et al., 2004a].

The possible sources for numerical balance error will now be discussed, together with methods implemented in Fluidity for tackling them. The Navier-Stokes equation for a Boussinesq flow in a rotating frame is:

$$\partial_t u + u \cdot \nabla u + 2\Omega \times u = -\frac{1}{\rho_0} \nabla p + g + \nu \nabla^2 u, \quad (3.1)$$

and the accompanying continuity (mass conservation) equation for an incompressible flow is:

$$\nabla \cdot u = 0, \quad (3.2)$$

where u is the Eulerian fluid velocity, Ω is rate of rotation with respect to an inertial frame, ρ_0 is the fluid reference density, p is pressure, g is buoyancy acceleration, ν is the kinematic viscosity and t is time. Equation 3.1 can be re-written as:

$$\partial_t u = -\frac{1}{\rho_0} \nabla p + F, \quad (3.3)$$

where:

$$F = -2\Omega \times u + g - u \cdot \nabla u + \nu \nabla^2 u. \quad (3.4)$$

Performing a Hodge-Helmholtz decomposition of the forcing terms F into a scalar potential ϕ and vector potential A [Ladyzhenskaya, 1969, Tong et al., 2003, Wiebel et al., 2004, Wu et al., 2006] gives:

$$F = \nabla \phi + \nabla \times A + H, \quad (3.5)$$

with boundary conditions $\nabla \phi \times n = 0$ and $(\nabla \times A) \cdot n = 0$ (where n is the unit normal). The conservative term $\nabla \phi$ is irrotational (curl free) while the rotational $\nabla \times A$ term is solenoidal (divergence free). The residual harmonic term, H , is both solenoidal and irrotational. Due to the continuity equation 3.2, the Eulerian acceleration $\partial_t u$ must itself be solenoidal. Hence, by 3.3, the pressure gradient term acts, and only acts, to filter the conservative component, $\nabla \phi$, of all forcing terms F . This demonstrates how only the rotational components of terms in the Navier-Stokes equation can influence the dynamics of the flow, and hence shows how the dynamics of incompressible flows can be entirely described using vorticity formulations in which the pressure gradient term is entirely absent.

Fluidity uses a pressure projection method to solve the Navier-Stokes equation, which is based upon this Hodge-Helmholtz decomposition method [Donea and

Huerta, 2003, Piggott et al., 2008]. In the pressure projection method a new velocity at time t^{n+1} , u_*^{n+1} , is computed using the old velocity at time t^n , u^n , from a discretisation of the Navier-Stokes equation 3.1, but using the pressure solution from the previous timestep, p^n . The pressure from t^n will not filter all conservative components of forcing terms at time t^{n+1} , and hence the resulting u_*^{n+1} will not be incompressible. Incompressibility is restored via a Hodge-Helmholtz decomposition of u_*^{n+1} :

$$u_*^{n+1} = u^{n+1} - \Delta t \nabla(\Delta p), \quad (3.6)$$

where Δt is the timestep and Δp is a pressure increment, $p^{n+1} = p^n + \Delta p$. Taking the divergence of this equation and imposing the incompressibility constraint $\nabla \cdot u^{n+1} = 0$ yields an elliptic problem for the pressure increment Δp . Hence in equation 3.6 u^{n+1} is the rotational component of u_*^{n+1} , while $-\Delta t \nabla(\Delta p)$ is the conservative component.

Now consider a system that is close to physical balance; to leading order the pressure gradient force is in near balance with the Coriolis force (geostrophic balance) and the buoyancy force (hydrostatic balance):

$$\frac{1}{\rho_0} \nabla p = -2\Omega \times u + g. \quad (3.7)$$

Note here that in order for such a balance to be possible the Coriolis and buoyancy forces must be (to leading order) pure conservative. Hence balanced states are irrotational, and a source of numerical balance error can be identified [Cotter, 2009a,b]: the balanced state may not be irrotational in the discrete space. If the balanced state is not (in the discrete space) irrotational, then the (discrete) pressure gradient can only act to filter its (discrete) conservative component, leading to an unphysical coupling between the balanced state and vortical dynamics. This is equivalent to saying that the balance equation 3.7 may not hold exactly in the discrete sense for a balanced flow.

There are two techniques implemented in Fluidity to enable accurate representation of physical balance. For the first technique, we decompose pressure into [Ford et al., 2004a, Pain et al., 2005, Piggott et al., 2008]:

$$p = p_g + p_r, \quad (3.8)$$

where p_g (referred to as the “balanced pressure” component) filters the conservative component of the Coriolis and buoyancy forces, while p_r (the residual pressure component) filters the conservative component of all other terms in the Navier-Stokes equation:

$$\frac{1}{\rho_0} \nabla p_g = (-2\Omega \times u + g)_{\text{conservative}}, \quad (3.9)$$

$$\frac{1}{\rho_0} \nabla p_r = (-u \cdot \nabla u + \nu \nabla^2 u)_{\text{conservative}}. \quad (3.10)$$

p_g can now be solved for by taking the divergence of equation 3.7 to form an elliptic problem:

$$\nabla^2 p_g = -\nabla \cdot (2\Omega \times u + g), \quad (3.11)$$

subject to the boundary condition $(\nabla p_g + 2\Omega \times u) \cdot n = 0$ on all boundaries. The Navier-Stokes equation then becomes:

$$\partial_t u + u \cdot \nabla u + 2\Omega \times u = -\frac{1}{\rho_0} \nabla p_r + g + \nu \nabla^2 u - \frac{1}{\rho_0} \nabla p_g, \quad (3.12)$$

where p_g is explicitly known, and hence the balanced pressure solver acts to precondition the pressure projection. One is now free to choose a general element choice for the balanced pressure component p_g , (noting that there is no limitation imposed here by the Ladyzhenskaya-Babuška-Brezzi stability condition - see Donea and Huerta [2003] for details). Hence, for the $P1 - P1$ element pair (piecewise linear for velocity, piecewise linear for pressure) a $P2$ (piecewise quadratic) element for p_g can be chosen - a choice which has the serendipitous property of being able to exactly represent hydrostatic balance for linear stratification. Note that, even with a piecewise quadratic element choice for balance pressure, the discrete balance pressure gradient does not map onto the discrete (piecewise linear) velocity space. Hence the balance pressure gradient is still not, in the discrete space (and in general), irrotational, and there is still a residual balance error. The balance pressure preconditioner method does not guarantee an *exact* discrete representation of physical balance - only a more *accurate* representation.

The second technique uses a mixed DG-CG element pair, $P1_D - P2$ [Cotter et al., 2009b,a, Comblen et al., 2009], whereby velocity is discretised using piecewise linear discontinuous basis functions while pressure is discretised using piecewise quadratic continuous basis functions. This element pair has the property that the gradient operator in the pressure space maps exactly onto the velocity space. From this it can be shown [Cotter, 2009a,b] that geostrophically balanced states are pure conservative in the discrete sense. This element choice is therefore optimally balanced, rather than simply giving a more accurate representation of balance.

At the time of writing the $P1_D - P2$ element pair is still at the implementation and testing stage. $P1_D - P2$ simulations of the annulus with ICOM are technically possible, but as it is still a highly developmental discretisation and has not been available for the entirety of this DPhil project, work in the DPhil to date uses the standard $P1 - P1$ element pair with a $P2$ balanced pressure preconditioner. A publication on the balanced pressure preconditioner method, including numerical benchmarks and geophysical examples, is currently in preparation.

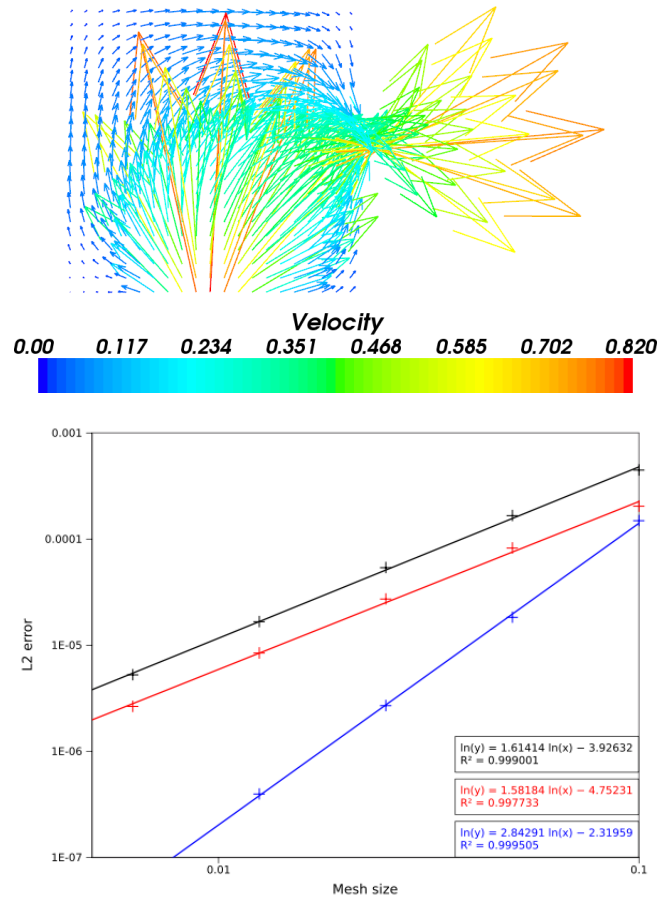


Figure 3.3: A simply connected barotropic source-sink flow on an f -plane for Reynolds number 1, Rossby number 12.5. These flows are in exact geostrophic balance everywhere and are unaffected by rotation [Taylor, 1917, Hide, 1997] (see section 5.1). Hence the difference between non-rotating and rotating simulations gives a measure of the discrete balance error, shown below for $P1 - P1$ (black), $P1 - P1$ with $P2$ balance pressure preconditioner (red), and the $P1_D - P2$ optimally balanced element pair of [Cotter et al., 2009b] (blue). Non-dimensional units.

Hence the balance pressure preconditioner method allows accurate (but not exact) representation of leading order balances even on arbitrarily unstructured meshes. This is an essential requirement for any simulation of the thermally driven annulus, and hence is a serious advantage offered by ICOM. However, it has not yet been shown that this accurate representation of balance is preserved when moving between meshes, as in dynamic mesh adaptivity. Hence there is a potential for coupling between balanced and vortical dynamics in mesh-to-mesh projections, and possibly for coupling between inertial modes and slow Rossby modes (higher order balance loss) when performing dynamic mesh optimisations.

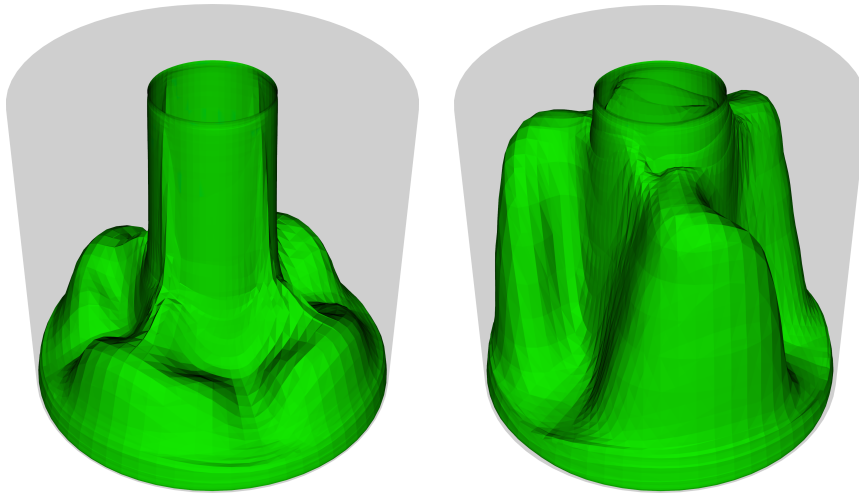


Figure 3.4: Left: A static mesh simulation of the thermally driven annulus using the $P1 - P1$ velocity-pressure element pair with a $P2$ balance pressure preconditioner (parameters as in table 4.1) for $\Omega = 2.674$ rad / s. $(T - T_A)/(T_B - T_A) = 0.5$ isosurface shown. Right: As left, but with the balance pressure preconditioner disabled. The former exhibits a stable mode four baroclinic wave, while the latter exhibits an unexpected strongly amplitude vacillating wavenumber three mode.

3.3 Mesh Adaptivity

As mentioned in section 3.1, there is an inherent computational cost associated with the move from structured meshes to unstructured meshes. While unstructured meshes have benefits in terms of their representation of boundaries, in order for unstructured simulations to compete with their structured mesh equivalents it is required that they in some way be able to make more efficient use of their degrees of freedom. The mechanism for this is mesh adaptivity - whereby the mesh resolution is non-uniform (and possibly anisotropic) throughout the simulation domain.

There are a number of techniques that can be applied in order to introduce mesh adaptivity:

- Adaptive mesh refinement (AMR);
- Edge- and face-wise element operations (h-adaptivity);
- Mesh perturbation and/or movement (r-adaptivity);
- Element-wise changes of element basis function order (p-adaptivity).

Adaptive mesh refinement uses nested grids of structured meshes, combining the benefit of concentrated mesh resolution with structured meshes. AMR can be implemented for finite difference models. In h-adaptivity, the topology of the mesh is altered to suit the simulation dynamics, whereas in r-adaptivity the topology of the mesh remains fixed while the nodal positions move through space (e.g. in a Lagrangian or “sprung nodes” type manner [Piggott et al., 2006]). In p-adaptivity the underlying physical mesh is fixed, while the order of the elemental basis functions is varied. Note that p-adaptivity and AMR can suffer from “hanging node” problems, although this can be overcome using discontinuous formulations.

In Fluidity adaptivity is controlled via an error (or adaptivity) metric that defines a Riemannian space [Piggott et al., 2006], within which an optimal element is measured to have unit size. Given an adaptivity metric the mesh is optimised through a combination of h- and r- type adaptivity, through local topological element operations and element perturbations [Pain et al., 2001]. Following the mesh optimisation the solution fields are “consistently” interpolated by evaluating the solution fields of the donor (old mesh) at the nodes of the target (new optimised mesh). Consistent interpolation is bounded, but not conservative nor strictly dissipative (aliasing errors can actually act as negative dissipation).

The primary mechanism for error metric formulation used by Fluidity is interpolation error driven - i.e. the metric relates to the interpolation error associated with the current mesh. From interpolation theory it follows that, for an element e , the inf-norm interpolation error ϵ in a field u is bounded by [Piggott et al., 2006]:

$$\epsilon_e = \|u - \Pi_h u\|_\infty \leq \hat{\gamma} \max_{x \in e} \max_{v | x+v \in e} (v^T |H(x)| v), \quad (3.13)$$

where Π_h is the Lagrange interpolant, $|H|$ denotes “eigenrecomposition with absolute value of H eigenvalues” (since positive and negative curvature should be treated equivalently), $\hat{\gamma}$ is some constant that depends on the dimension and element geometry, H is the Hessian (tensor of second derivatives), x is a coordinate in the element e and v is some displacement relative to x that is also in element e . Hence interpolation error driven adaptivity is equivalent to field curvature driven adaptivity. An interpolation error metric therefore has the form:

$$\hat{M} = \frac{|H|}{\hat{\epsilon}}, \quad (3.14)$$

for some given $\hat{\epsilon}$ determining the adaptivity sensitivity, and this error metric can now be used to drive adaptivity. Note that in the error metric formulation 3.13 is defined from the inf-norm interpolation error. This will selectively resolve only the regions of highest curvature in the simulation [Alauzet et al., 2006]. More advanced metric formulations are possible - for example based upon more general norms [Zienkiewicz and Zhu, 1991, Alauzet et al., 2006] or using goal

based (or sensitivity driven) adaptivity metrics [Power et al., 2006]. The former has only very recently become available for ICOM simulations, while the latter requires an adjoint model (which ICOM is currently lacking). Hence adaptive simulations to date make use of the inf-norm interpolation error metric.

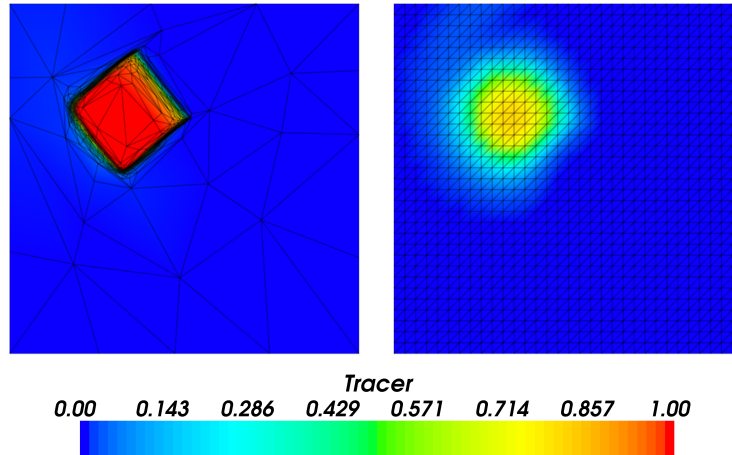


Figure 3.5: Left: An adaptive mesh ICOM simulation of a top hat advected with solid body rotation (in the anti-clockwise sense), with 1139 nodes. Right: A similar static mesh ICOM simulation, with 1089 nodes. The implicit numerical diffusion in the latter is clear.

For the purposes of simulations of the thermally driven annulus, dynamic mesh adaptivity gives an opportunity to conduct simulations in more exotic annulus regimes containing multi-scale physics where the location of interesting or physically important regions of the flow cannot be predicted a priori, and for which the global refinement capable of resolving these features would be ruinously computationally expensive. It also has the potential to simulate the annulus at a higher accuracy for a given computational cost, leading to a closer representation of experiment [Farrell, 2008]. However, it is currently unproven in a geophysical context. In particular, it has yet to be established that metrics based upon numerical accuracy (such as the inf-norm interpolation error) are appropriate. Also, the influence of mesh-to-mesh projections on geophysical simulations has yet to be determined.

A paper detailing the parallel implementation of the ICOM mesh optimisation procedure has recently been submitted using the annulus as a numerical benchmark.

3.4 Summary

Key technologies implemented in Fluidity and of relevance to simulations of the thermally driven annulus have been discussed. The benefits of unstructured

mesh simulations have been identified, and include the ability to conform to bounding topography and their suitability for the application of dynamic mesh adaptivity. Potential problems with the use of unstructured meshes include issues with wave propagation through resolution gradients, issues with accurate representation of physical balance, and computational cost. Techniques for the solution of the latter two of these issues were supplied, with balanced pressure preconditioner and optimally balanced element methods for the former, and dynamic mesh adaptivity methods for the latter.

A remaining issue of key relevance to simulations of the thermally driven annulus is that, while many of the technologies implemented in Fluidity have been proven in a CFD context, many remain unproven in a geophysical context. A consequence of this is that there is generally a lack of accepted geophysical adaptivity metrics and mesh-to-mesh projection validation. The following chapter will detail work undertaken in this DPhil project to validate key Fluidity technologies, and to identify strengths and weaknesses with Fluidity methods.

Chapter 4

Model Validation

While the key model advantages offered by ICOM described in the previous chapter undoubtedly have promise for new, more detailed and more accurate simulations of the thermally driven annulus, there are a number of potential issues associated with transferring the techniques from the field in which they were developed, primarily a CFD context, to the field of simulations of geophysical fluids.

This chapter details work on validation of ICOM as a model for the thermally driven annulus when run using a static structured mesh. It further details the validation of the technique of fully unstructured dynamic mesh adaptivity, in order to identify potential issues with its translation from a CFD context to simulations of the thermally driven annulus.

Recently, a coding error in the CFL number diagnostic (used to choose the timestep for adaptive timestepping) was identified. Hence there are some inconsistencies between the earlier simulations (used for figures 4.2, 4.3, 4.4, 4.8, 4.10 and 4.12) and more recent simulations (used for figures 4.5, 4.6, 4.7 and 4.11). The heat transport validation suite is being repeated in order to resolve this issue. However, this issue is not expected to significantly alter the conclusions of this chapter.

4.1 Verification versus Validation

There are, broadly speaking, three key requirements in assessing the performance of a model code:

1. Model verification;
2. Model validation;

3. Model performance.

Point 1 assesses and asserts that the numerical model is an implementation of the underlying numerical schemes; it assesses purely that there are no implementation flaws that have been introduced in translating numerical schemes from paper to program. A particularly powerful example of this is the “method of manufactured solutions” (MMS) [Salari and Knupp, 2000, Roache, 2002, Farrell et al., 2008], in which one selectively chooses model parameters so as to artificially construct an analytically soluble equation, thereby ensuring consistency of the numerical solution with respect to the continuous equations. Model verification is an essential step in the implementation of a numerical model, but is insufficient for the purposes of physical application. It is, trivially, a necessary requirement of a model, but it does not in any sense guarantee that the model gives us a useful representation of the physical world - atmosphere or ocean models are rarely run to convergence and are usually, due to limitations on computational resources, run at their very limits of stability and resolution. Hence point 2, model validation, in which an application of a numerical model is applied directly to simulations of physical systems. This is qualified by point 3; it is not useful for it to be merely theoretically possible for a model to be applied to a system - the model must instead be capable of reproducing the key physical system properties when used with a realistic (and ideally competitive) configuration.

Whilst validation against existing models is certainly a useful approach, the real strength of the annulus as a geophysical test case is its wealth of previous laboratory research. Hence the validation focuses on comparison of numerical simulations with existing laboratory data.

4.2 Heat Transport Validation

As a first step we seek to validate the global performance of the representation of the dynamics of the thermally driven annulus by ICOM. Such a useful global measure is the system heat transport, conveniently defined via the non-dimensional Nusselt number expressing the heat transport integrated over some surface as compared to the heat transport of a solid of equal conductivity to the fluid. Integrating over the annulus inner wall this gives [Read, 2003]:

$$Nu = \frac{H \ln(b/a)}{2\pi \kappa d \rho_0 c \Delta T}, \quad (4.1)$$

where H is the heat transport (a power), a , b and d are as in figure 2.2, κ is the system diffusivity, ρ_0 is the reference density, c is the specific heat capacity, and ΔT is the tank thermal forcing. A system Peclet number defining the normalised advective heat transport is given by $Pe = Nu - 1$. Re-writing this in a more diagnostically useful form:

$$Nu = \frac{\ln(b/a)}{2\pi d\Delta T} \int \nabla T \cdot dn. \quad (4.2)$$

Noting that, as described in section 3.1, finite element methods define the solution over the entire computational domain, this integral can be performed exactly from the model solution:

$$Nu = \frac{\ln(b/a)}{2\pi d\Delta T} \sum_{i,j} T_i \frac{dN_i}{dx_j} \cdot dn_j, \quad (4.3)$$

where N_i are the elemental basis functions, T_i are the nodal temperature values and n_i are the element surface normals. Hence system heat transports can be diagnosed for arbitrary unstructured meshes. This diagnostic has itself been verified using the cavity convection numerical benchmark of de Vahl Davis and Jones [1983], shown in figure 4.1. Null testing (for pure diffusive flows, and for no-flux boundaries of annulus simulations) indicate that this diagnostic is accurate to $\sim 1\%$ for typical annulus simulations with ICOM.

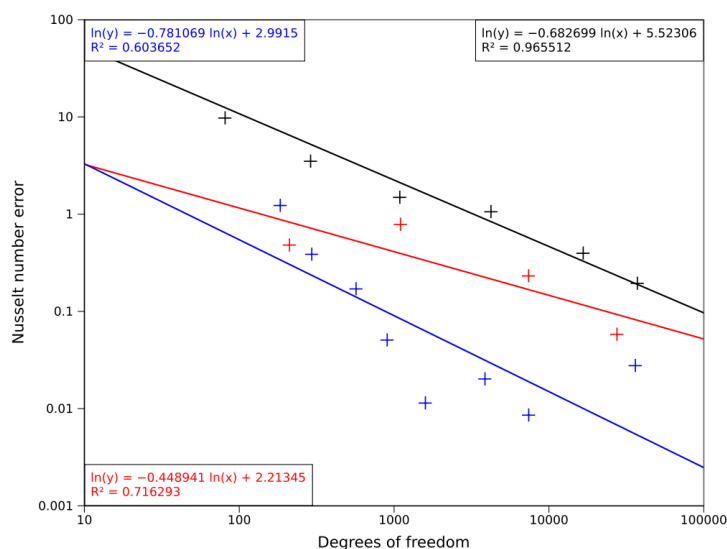


Figure 4.1: Convergence testing using ICOM of the Nusselt number diagnostic defined by equation 4.2, tested against the de Vahl Davis and Jones [1983] Prandtl number 0.71 cavity convection benchmark at Rayleigh number 10^6 . Uniform mesh simulations are shown in black, and inf-norm interpolation error driven (as in equation 3.13) mesh adaptive simulations are shown adapting to the temperature field in red, and adapting to the velocity field in blue.

For the standard open tank thermally driven annulus with a rigid lid, the contributions to the system heat transport are: flux through the Ekman layers,

ventilation by the interior baroclinic eddies, and diffusion. At very low rotation rate and for annulus parameters ($Ra \sim 10^7$) an additional convective overturning is expected, characteristic of natural convection. A more detailed discussion of these transport mechanisms, and transitions between natural convection and Ekman layer transport regimes, is given in Read [1992].

It has previously been noted that once baroclinic eddies are allowed to develop the system heat transport is observed to remain remarkably close to its non-rotating value through a number of regime and wavenumber transitions [Read, 2003]. In this way the baroclinic wave can be considered a ventilation mechanism whereby the system adds, at increasing rotation rate, additional eddies in order to maintain its non-rotating advective transport.

There are therefore a number of benefits in using the system heat transport for model validation. It is dependent upon a range of physical processes and hence is sensitive to: poor representation of boundary layers, poor representation of advection, and poor representation of the dynamics of baroclinic instability. All of these must be captured in order to give a (consistently) good measured heat transport. It is also expected that the system heat transport should, for non-turbulent regimes, remain confined to a relatively narrow range of values. In addition to this it is a single value including information about the global system dynamics, greatly aiding comparison.

4.3 Static Structured Mesh Simulations

Static structured mesh simulations were conducted with system parameters as given in table 4.1. Rather than using a uniform mesh, it was decided that the two directional tanh stretch mesh of Farnell and Plumb [1975, 1976], resolving both the buoyancy and Ekman boundary layers, would be used. The static mesh had a resolution of $24 \times 24 \times 64$ nodes in radius, depth, and azimuth respectively. This mesh choice enables a comparison of adaptive mesh methods with a pre-existing and accepted a-priori adapted mesh. The model configuration details were: centred $P1 - P1$ (piecewise linear for velocity and pressure) CG discretisation for momentum with $P2$ balanced pressure preconditioner to increase balance accuracy, and CV discretisation for temperature with Sweby limiter to avoid artificial numerical stratification as a result of over- and under-shoot errors. An implicit Crank-Nicholson timestepping scheme was used [Piggott et al., 2008] with an a-posteriori adaptive timestep targeting a maximum Courant-Friedrichs-Lewy number [Courant et al., 1928] of 2.5. Early simulations were initialised using output from the MORALS model¹ from non-matched physical parameters, in order to decrease model spin-up time. More recent simulations are significantly faster as a result of ongoing ICOM optimisations, and hence later simulations are initialised with no-flow and internal linear stratification. The model was integrated for a nominal simulation time of 2000s to 4000s. As a result of the extremely long run-time of these simulations, typically lasting several processor weeks, many were terminated prior to reaching

¹Courtesy Roland Young

simulation completion. Simulations at rotation rates of $\Omega \geq 3.513$ rad / s were observed to be numerically unstable in a manner consistent with advective instability of the momentum discretisation. No upwind stabilisation schemes were available at the time of these simulations, and hence rotation rates are limited to the range $\Omega = 0.608$ rad / s to $\Omega = 2.764$ rad / s.

Table 4.1: Parameters used for simulations of the standard thermally driven annulus. These parameters correspond to those used in Read [2003].

Parameter	Symbol	Value
Minor radius	a	2.5 cm
Major radius	a	8.0 cm
Depth	d	14.0 cm
Thermal forcing	$T_B - T_A$	4 K
Kinematic viscosity	ν	1.3×10^{-2} cm ² / s
Thermal diffusivity	κ	1.03×10^{-3} cm ² / s
Thermal expansion coefficient	α	3.3×10^{-4} / K
Gravitational acceleration	g	981 cm / s ²
Rotation rate	Ω	0.608 to 2.764 rad / s
Prandlt number	Pr	14
Thermal Rossby number	Θ	1.6 to 0.078
Taylor number	Ta	1.2×10^6 to 2.5×10^7

The numerical simulations were compared directly against laboratory heat flow annulus data for matching physical parameters [Read, 2003]. Laboratory measurements of the system heat transport are quoted to be accurate to within an error of $\pm 2.5\%$ [Read, 2003]. The laboratory system contained an in-situ thermocouple array.

An overview of the observed baroclinic wave modes for these simulations is given in figure 4.2. The wavenumber transition regions are consistent with those observed in experiment. There is also evidence of amplitude vacillation, particularly in the region immediately surround the 2/3 mode transition. An overview of the final system heat transport for these simulations is given in figure 4.4.

The simulated system heat transport is observed to be broadly consistent with the laboratory measurements. In particular, the simulated heat transport is, as expected, very nearly uniform throughout the range of rotation rates simulated, consistent with a baroclinic wave ventilation mechanism. Furthermore, the simulated heat transport is within experimental errors bars for 4 of the 10 simulations. There is some evidence for a decrease in the simulated heat transport for the highest rotation rates, possibly an indication of decreasing model stability at increased Reynolds numbers. Since it is known that the system heat transport is rather difficult to reproduce in numerical simulations, ICOM is judged to be performing well for this diagnostic in the steady wave annulus regime.

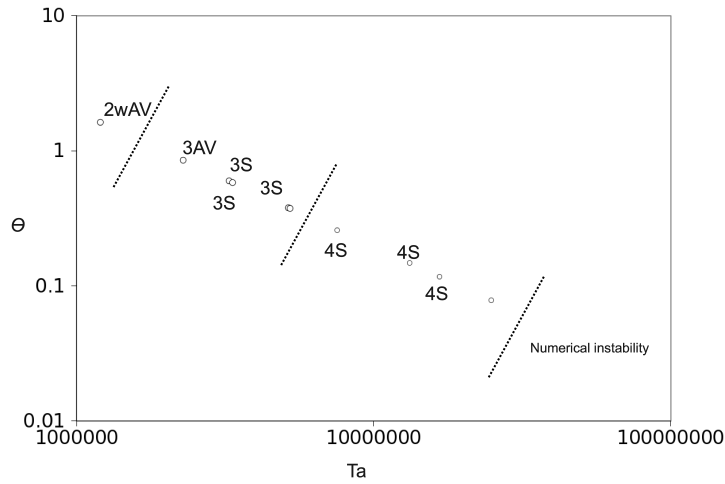


Figure 4.2: Sketch regime diagram for the static mesh ICOM simulations of the thermally driven annulus, indicating a series of wavenumber transitions. S = steady wavenumber mode, AV = amplitude vacillation, wAV = weakly amplitude vacillating.

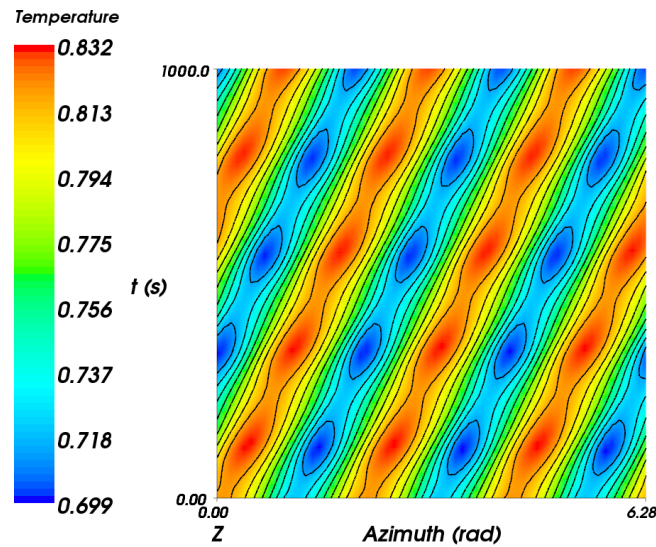


Figure 4.3: Hovmöller plot formed from the mid-point ($r = 5.25$ cm, $z = 7.0$ cm) temperature field for a static mesh ICOM simulation of the thermally driven annulus at $\Omega = 0.838$ rad / s. Normalised temperature $(T - T_A)/(T_B - T_A)$ shown. This simulation exhibits a wavenumber 3 amplitude vacillating mode.

4.4 Adaptive Mesh Simulations

The static mesh configuration was altered to use an anisotropic dynamically adaptive mesh. Adaptivity metric tolerances ($\hat{\epsilon}$ in equation 3.14) were chosen

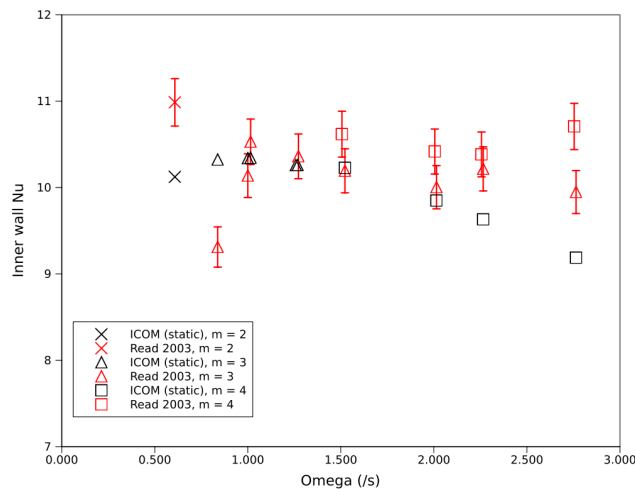


Figure 4.4: Heat transport measurements for fixed mesh ICOM simulations of the thermally driven annulus annulus (black) and experimental observations (red). Here m denotes the wave number (cross = wave number 2, triangle = wave number 3, square = wave number 4).

for all three components of velocity, for temperature, and for the “balance pressure” component of pressure. The metric tolerances were chosen so as to give a good, by eye, mesh for the $\Omega = 1$ rad / s simulation, and were then scaled according to field magnitudes for all other simulations. Consistent interpolation was used for all fields, and mesh adapts performed every 20 timesteps. Many of the dynamically adaptive meshes generated contained many more degrees of freedom when compared to their static mesh equivalents. Hence the simulated times for the adaptive mesh simulations were generally considerably lower than the static simulations. However, it was noted from the static simulations that the system heat transport generally approached close to its final value relatively early in the simulation, once the baroclinic wave had developed. Hence the reduced simulation time is not expected to have a significant influence on the final measured system heat transport.

An example of the system heat transport for an $\Omega = 1$ rad/s simulation is given in figure 4.7. There is an unfavourable comparison of the system heat transport both against experiment and against the static simulations, indicating a 1.2, or $\sim 10\%$, decrease in the normalised system heat transport. This is in addition to the static simulation having only 36864 degrees of freedom, and the adaptive having an average of 65973. Hence, even discounting the not insignificant cost of error metric assembly, mesh adaptivity and parallel re-load-balancing, the adaptive simulation is nearly twice as expensive as the static simulation, and has a decreased accuracy with respect to the heat transport diagnostic. This result extends across the whole range of rotation rates, and shown in figure 4.8. Hence, ICOM in full anisotropic mesh adaptive mode is judged to be performing relatively poorly for this diagnostic in the steady wave annulus regime and for

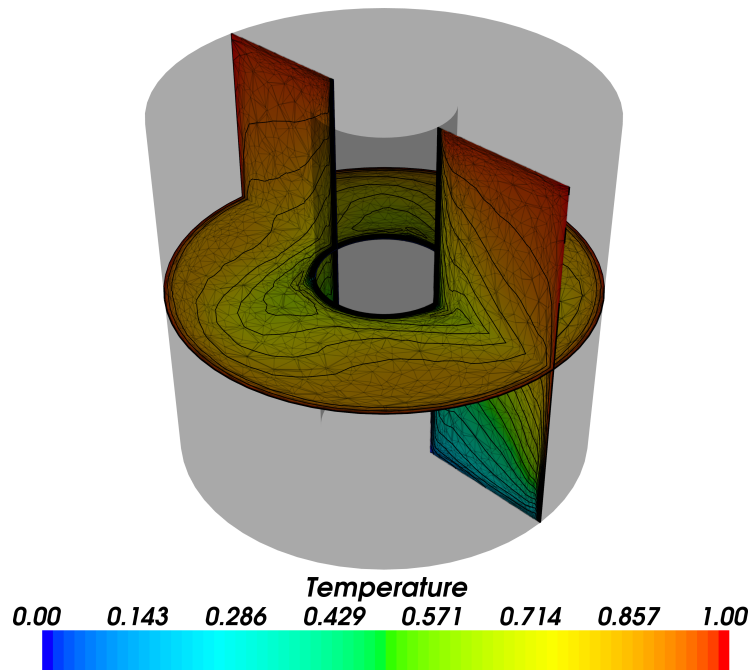


Figure 4.5: Adaptive mesh ICOM simulation of the thermally driven annulus at rotation rate $\Omega = 1$ rad / s. Showing normalised temperature $(T - T_A)/(T_B - T_A)$ with 20 contours, slicing through the annulus horizontally and vertically.

this configuration.

4.5 Mesh Adaptivity Errors

Mesh adaptivity is a four stage process:

1. Assembly of an adaptivity (or quality) metric from the solution fields;
2. Optimisation of the simulation mesh based upon that adaptivity metric during a mesh adapt;
3. Projection of the simulation fields from the original, sub-optimal, mesh to the new, optimised, mesh;
4. (In parallel) Re-load-balancing to re-distribute the problem across processes.

Hence from this two possible causes for the decrease in performance as measured against laboratory heat transport data can be identified: the mesh adaptivity

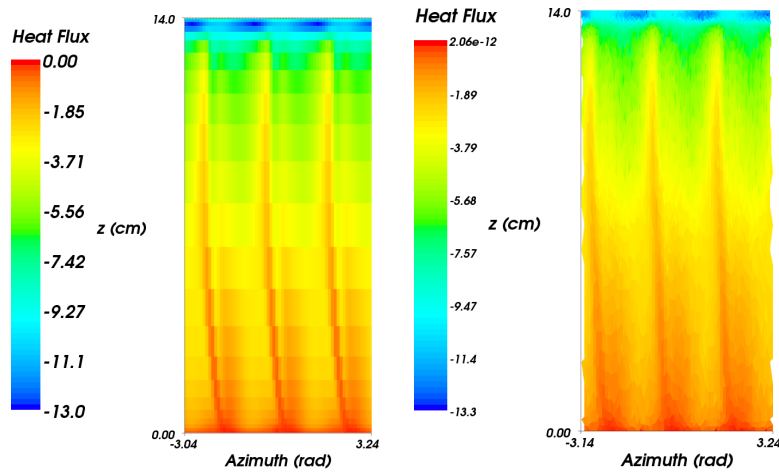


Figure 4.6: Inner wall heat fluxes for ICOM simulations of the thermally driven annulus at $\Omega = 1$ rad / s. Left: Static mesh simulation. Right: Dynamic mesh adaptive simulation. Displayed flux is $(\nabla T \cdot n) / (T_B - T_A)$ in units of /cm, with negative indicating flux out of the domain. The intense localised Ekman layer transport is clearly visible in the upper region, and the influence of the baroclinic wave on the thermal boundary layer can be seen forming a banded mode three structure in the lower region.

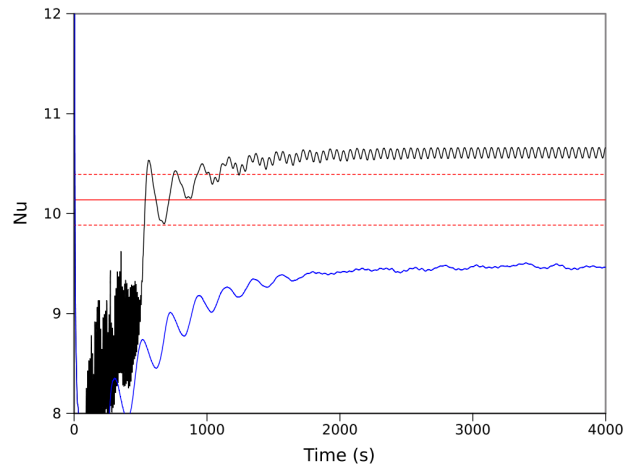


Figure 4.7: Heat transport measurements for $\Omega = 1$ rad / s simulations of the thermally driven annulus. The static mesh transport is shown in black, the adaptive mesh in blue, and laboratory measurement in red (with error bars).

metric may be unsuitable and give a reduced accuracy when compared to the manually optimised Farnell and Plumb [1975, 1976] tanh stretch mesh, or the

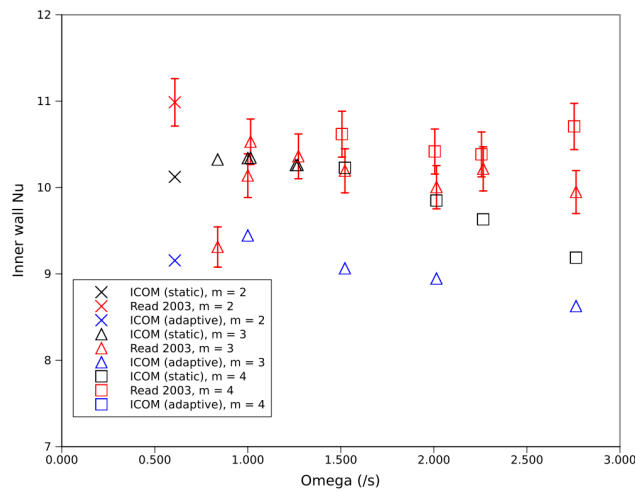


Figure 4.8: Heat transport measurements for adaptive mesh ICOM simulations of the thermally driven annulus annulus (blue) and experimental observations (red). Comparable static mesh simulations are shown in black. Here m denotes the wave number (cross = wave number 2, triangle = wave number 3, square = wave number 4).

mesh-to-mesh projection may introduce additional errors in the simulation. In addition to this, it is possible that the converged model solution differs from the laboratory solution, perhaps as a result of the presence of in-situ thermocouples in experiment.

A series of simulations were conducted in order to determine which of these is the cause of the reduced measured heat transport in adaptive mesh ICOM simulations. First, an adaptivity metric was formed directly from the Farnell and Plumb [1975, 1976] tanh stretch mesh, via a polar decomposition of the Jacobian matrices mapping elements to the unit tetrahedron [Micheletti and Perotto, 2006]. From this metric a new mesh of locally equal resolution to the structured tanh stretch mesh was generated using the mesh optimisation library. This process was iterated to generate ten such unstructured meshes, thereby giving ten meshes of locally equal resolution. ICOM was then instructed to “flick” between these meshes at 20 timesteps intervals. The flicking simulation was observed to be polluted with high frequency noise, and yielded an unstable wavenumber five mode. A comparable static mesh simulation yielded a wavenumber four mode. The heat transport for this simulation is shown in figure 4.10. Here it can be seen that the mere act of changing between meshes of locally equal resolution leads to a drop in the measured system heat transport.

A second simulation was conducted using the final, optimised, mesh from a full dynamically adaptive simulation. A simulation was then conducted using this mesh in static mode. The resulting simulation is shown in figure 4.11. Note a small increase in the measured system heat transport.

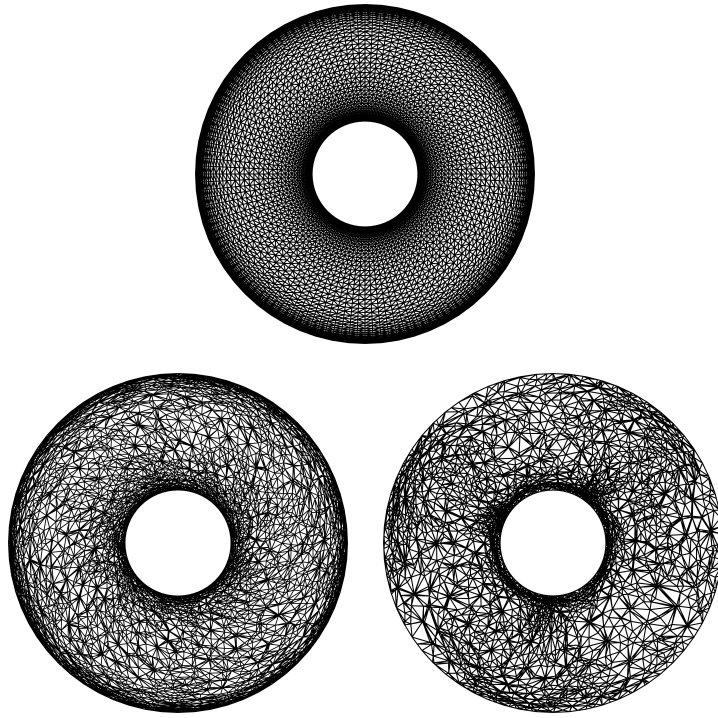


Figure 4.9: Above: Farnell and Plumb [1975, 1976] tanh stretch mesh at $\Omega = 2.764$ rad / s. Lower left: An unstructured mesh of locally equal resolution to the tanh stretch mesh. Lower right: Mesh from a dynamically adaptive ICOM simulation at $\Omega = 2.764$ rad / s.

From these simulations it seems likely that the influence of the adaptivity metric can be discounted as a direct cause of inconsistency with experimental observations. Very recently, high resolution simulations have shown a decrease in measured heat transport. Hence it is possible that there is a difference between the converged model solution and experimental observations. Further simulations are needed to investigate this. Despite this, the equal resolution mesh “flicking” simulation and the static simulation using a final adapted mesh show that there is a non-negligible effect on the measured system behaviour purely as a result of the mesh-to-mesh projection used in mesh adaptivity.

4.6 Mesh Projections

At the start of this project the only mesh-to-mesh projection available in adaptive mesh ICOM simulations was consistent interpolation (see section 3.3). This is advantageous in that the projection method is computationally cheap but, as discussed previously, the method is not conservative nor strictly dissipative.

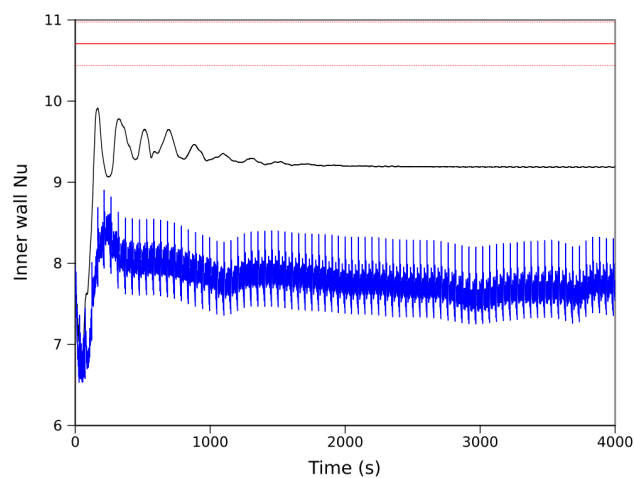


Figure 4.10: Heat transport measurements for a locally equal resolution mesh “flicking” simulation of the thermally driven annulus for $\Omega = 2.764$ rad / s (shown in blue) and a comparable static mesh simulation (black). Note that these simulations did not have the same dominant wavenumber - the flicking simulation was an unstable wavenumber five, while the static mesh simulation was a stable wavenumber four. A comparable laboratory measurement for a wavenumber four simulation in shown is red (with error bars).

As a result of the evidence presented in the previous section for the influence of mesh-to-mesh projections on adaptive mesh annulus simulations, work was undertaken to create a more suitable projection method. The method implemented is an extension of the Galerkin projection via supermesh construction described in Farrell et al. [2009]. This method solves the equation $A = B$ via Galerkin projection:

$$\sum_j N_i N_j A_j = \sum_j N_i M_j B_j, \quad (4.4)$$

where N_i are the elemental basis functions on the target mesh, M_i are the elemental basis functions on the donor mesh, and A_i and B_j are the nodal values of A and B respectively. The “mixed mass” contribution $N_i M_j$ must be formed via a numerical quadrature that can integrate, with zero numerical error, piecewise polynomials defined over intersecting elements. Since finite elements are essentially a method for performing integrals over complicated domains, this numerical quadrature can be performed by, for each element in the donor mesh, generating a “supermesh” containing all nodes and faces from the target that intersect with the donor element. Farrell et al. [2009] describes a method for constructing global supermeshes, that is, the intersection of all donor element with all target elements, implemented in 2D. The construction of a global supermesh for 3D simulations would be extremely computationally

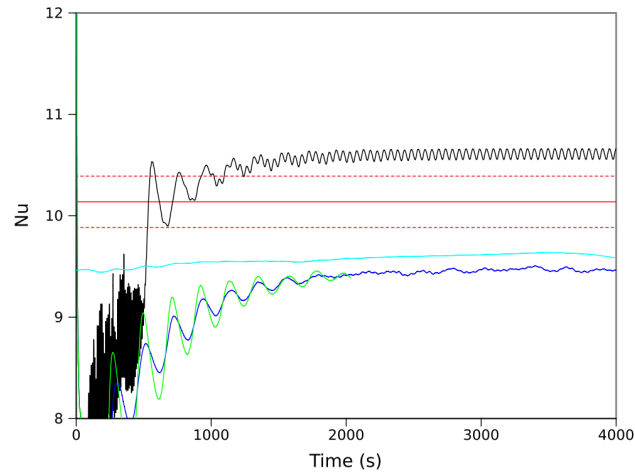


Figure 4.11: Heat transport measurements for $\Omega = 1$ rad / s simulations of the thermally driven annulus. The static mesh transport is shown in black, adaptive mesh with consistent interpolation in dark blue, adaptive mesh with conservative Galerkin projection in green, a static mesh simulation using a final adapted mesh in light blue, and the laboratory measurement in red (with error bars).

expensive. Hence this method has since been extended to use local (element-wise) supermeshing, and has also been extended to 3D. A publication detailing this method and its application to annulus simulations is in preparation.

Galerkin projection is a conservative projection method that minimises the mean square error between the donor field and projected field. The method is not bounded, but this failing can be tackled using minimally diffusive bounding methods as described in Farrell et al. [2009].

An adaptive mesh annulus simulation using Galerkin projection is shown in figure 4.11. It can be seen that, whilst the simulation using Galerkin projection is smoother than the consistent interpolation equivalent, the system heat transport is largely unaltered.

4.7 Balance Considerations

Figure 3.4 shows static mesh simulations conducted with and without the $P2$ balance pressure preconditioner, discussed in depth in section 3.2. The simulation without the balance pressure preconditioner exhibits a strong amplitude vacillating wavenumber three mode, while the simulation using the balance pressure preconditioner exhibits a stable wavenumber four mode. Comparing the heat transports for these two simulations (seen in figure 4.12), it can be seen that

the simulation without the balance pressure preconditioner has an enormously reduced simulated heat transport. Hence it is possible that the failure to take leading order balance into account when performing mesh-to-mesh projections, even the conservative Galerkin projection method described in the previous section, may be a significant cause of the reduced simulated heat transport for adaptive mesh simulations. It is therefore possible that a decomposition method, possibly based upon the Hodge-Helmholz decomposition method as for the balance pressure preconditioner, may have some benefits for these simulations.

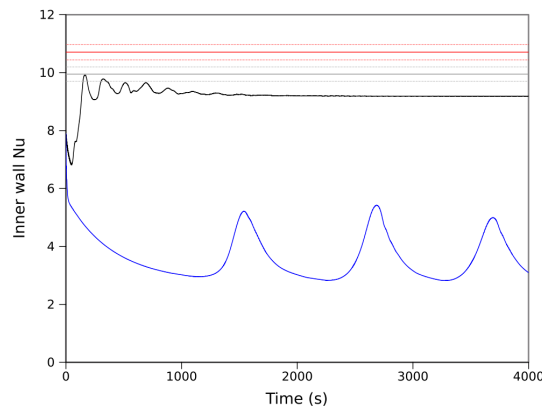


Figure 4.12: Heat transport with (black) and without (blue) the $P2$ balance pressure preconditioner for $\Omega = 2.674$ rad / s simulations of the thermally driven annulus. The former exhibits a stable wavenumber four, while the latter exhibits an amplitude vacillating wavenumber three. Wavenumber three and four laboratory observations are shown in grey and red respectively (with error bars). The heat transport of the simulation with balance pressure disabled is unphysically low for these system parameters.

4.8 Summary

The thermally driven annulus has been simulated using ICOM with both a priori adapted tanh stretch static meshes and full dynamic mesh adaptivity. The static mesh simulations are seen to compare well to laboratory observation of the system heat transport, while the adaptive mesh simulations are seen to compare relatively poorly. Further testing has revealed that mesh-to-mesh projections alone can be responsible for reductions in the simulated heat transport. A conservative projection mechanism was developed and applied to the annulus, but this shows little benefit in terms of the measured system heat transport.

In order for more concrete conclusions to be drawn, further work will focus on comparing other system diagnostics with experiment. In particular, in-situ

thermocouple measurements are available for all of the configurations simulated. The amplitude of the wave modes in numerical simulations will be compared directly against laboratory values. In addition to this, higher resolution static simulations are required for a sample of rotation rates, in order to determine (as closely as possible) converged model values for the important diagnostic quantities.

Chapter 5

The Radial Barrier Annulus

One of the defining characteristics of the standard annulus configuration, as shown in figure 2.2, is that the tank geometry is multiply connected. From an oceanographic point of view the dynamics of the open annulus is therefore more an analogue of the Antarctic Circumpolar Current than it is, say, an oceanic gyre [Wordsworth, 2008].

In this chapter we discuss ICOM simulations of the rotating annulus with a full radial barrier. This apparently rather subtle change to the system geometry has a dramatic change on the physics of the system, as we move from a multiply connected to a simply connected topology. This system has also, as discussed in section 2.4, previously been challenging to simulate numerically.

5.1 Topological Effects

Consider a barotropic annulus with an inner and outer wall source-sink flow. In the standard open case the radial flow induced by the source-sink forcing is subject to an azimuthal Coriolis force. However, as a result of the topology, there is no single-valued pressure gradient that can balance this Coriolis force in the azimuthal direction. Hence even irrotational components of the Coriolis force in the azimuthal direction can not be filtered by the pressure gradient term - there is a harmonic residual component to Coriolis (see section 3.2). This barotropic source-sink flow on an f -plane is affected by rotation, [Hide, 1968, 1997]. In contrast, once one adds a full radial barrier a pressure gradient can be supported and still be single-valued, with a corresponding pressure drop across the radial barrier supporting exact geostrophic balance in the interior - a principle used to derive the numerical balance errors in figure 3.3 [Taylor, 1917, Hide, 1997]. This effect is shown in figure 5.1.

Extending this principle to baroclinic fluids one finds (discussed in detail in Hide

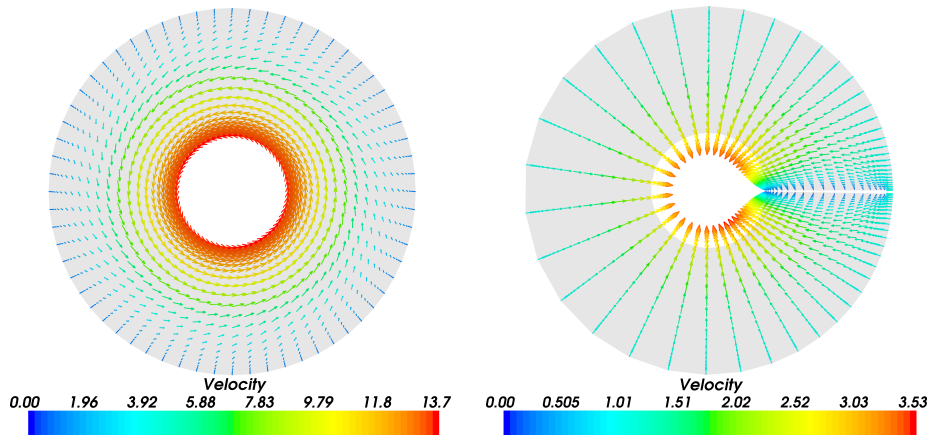


Figure 5.1: Left: ICOM simulation of a low Reynolds number (~ 10) open source-sink barotropic rotating annulus (normal inflow at outer wall, outflow at inner wall), exhibiting a “corkscrew” flow as a result of the harmonic Coriolis residual (velocity vectors shown). Right: As left, but with the insertion of a thin (1 degree) full radial barrier. In this case the flow is unaltered by the system rotation with a direct radial geostrophic flux being supported by a pressure drop across the barrier. Note that both cases are zero vorticity flows, but only the latter has Ω independent boundary conditions for the vorticity equation [Hide, 1968]. Simulation details: $a = 2.5$, $b = 8.0$, $\nu = 1.0$, unit inflow.

[1997]) that the non-rotating solution cannot be a solution in the rotating case for an open annulus - a consequence of the absence of a Stokes’ theorem for this topology. However, for a simply connected annulus domain the non-rotating solution is, by simple circulation arguments, a possible solution in the rotating case. Through thermal wind arguments [Rayer et al., 1998], an azimuthal temperature gradient can be generated that acts to balance the azimuthal Coriolis force:

$$g\alpha \frac{1}{r} \frac{\partial T}{\partial \phi} = -2\Omega \frac{\partial v}{\partial z}, \quad (5.1)$$

where here ϕ is the azimuthal coordinate, r is the radial coordinate, z the vertical coordinate, and v is the radial component of Eulerian velocity. This does not mean that the dynamics will select this solution - merely that it is permitted. This leads to the hypothesis that, with the introduction of a radial barrier, a compensating temperature field (and hence, through hydrostatic balance, a corresponding pressure field) may be established that acts to filter the influence of rotation from certain system features, and in particular to maintain the system heat transport at its non-rotating value. This hypothesis is supported by the experiments detailed in Rayer [1992] and Rayer et al. [1998]. In Hide [1997] a further hypothesis is made concerning the flow relative potential vorticity:

$$\zeta = \omega \times \nabla\Theta, \quad (5.2)$$

where ω is the relative vorticity and Θ is, in this context, the potential temperature. It is postulated that there will exist a flow regime within which the flow relative potential vorticity will maintain its non-rotating value (of zero), and hence this can be used diagnostically to determine the influence of rotation on the system. This is very tentatively supported by the two orthogonal η and ζ circulations observed in the baroclinic radially blocked annulus experiments of Rayer [1992], which contribute with opposite sign to the relative potential vorticity.

5.2 ICOM Simulations of the Radially Blocked Annulus

The configuration used in chapter 4 was modified to simulate an annulus with a one degree insulating full radial barrier. The $24 \times 24 \times 64$ Farnell and Plumb [1975, 1976] tanh stretch mesh was altered to give a tanh stretch mesh in all three dimensions in order to resolve any radial barrier boundary layer effects. ICOM was run in static mesh mode using parameters as given in table 5.1, for two different Prandtl number fluids and for rotations rates of $\Omega = 1$ rad / s to $\Omega = 10$ rad / s.

Table 5.1: Parameters used for simulations of the full radial barrier annulus. Two fluids were used, with the Prandtl number 14 fluid corresponding to that used in experiment Rayer et al. [1998].

Parameter	Symbol	Value
Minor radius	a	2.5 cm
Major radius	a	8.0 cm
Depth	d	14.0 cm
Thermal forcing	$T_B - T_A$	4 K
Kinematic viscosity	ν	1.81×10^{-2} cm ² / s
Thermal diffusivity	κ	1.03×10^{-3} cm ² / s and 5.18×10^{-3} cm ² / s
Thermal expansion coefficient	α	3.03×10^{-4} / K
Gravitational acceleration	g	981 cm / s ²
Rotation rate	Ω	1 to 10 rad / s
Prandtl number	Pr	14 ($\kappa = 1.03 \times 10^{-3}$ cm ²) and 3.5 ($\kappa = 5.18 \times 10^{-3}$ cm ²)
Thermal Rossby number	Θ	0.55 ($\Omega = 1$ rad / s) to 0.0055 ($\Omega = 10$ rad / s)
Taylor number	Ta	4.4×10^6 ($\Omega = 1$ rad / s) to 4.4×10^8 ($\Omega = 10$ rad / s)

Figure 5.2 shows an example of these simulations, with comparison figures from laboratory experiments from Rayer [1992] and with previous numerical experiments from Rayer [1992, 1994]. The ICOM simulations give a good qualitative representation of the flow. Overturning and barotropic streamfunctions for the $\Omega = 1$ rad / s simulation for the Prandtl number 14 fluid are shown in figure 5.4. These clearly show the presence of a meridional overturning circulation (the η circulation of Rayer et al. [1998]) and a horizontal boundary circulation (the ζ circulation). However, there are significant deviations from the experimental flow pattern towards the tank inner wall - these deviations are similar in nature to those seen in previous numerical simulations. There is a distinct banding, with the azimuthal flow sign changing twice in the inner wall region. This could be a numerical error due to insufficient mesh resolution in this region, or due to the presence of in-situ thermocouples acting to change the effective experimental parameters. There were also, for some of the simulations, small scale eddies within this strongly sheared inner region of the flow. These have previously been attributed to model resolution effects - they were seen in the numerical simulations of Rayer [1992], and have also been seen in open tank simulations, but tend to appear at only certain (intermediate) mesh resolutions [White, 1988].

The $\Omega = 10$ rad / s simulation was observed to be numerically unstable for the Prandtl number 14 fluid, and is excluded from further analysis. Short-lived eddies, of a similar nature to the baroclinic eddies observed in open annulus geometries, were observed for the Prandtl number 14 fluid, but these all dissipated by simulation end. In contrast to this, long-lived eddies were observed for all of the Prandtl number 3.5 fluid simulations.

5.3 Heat Transport

The heat transport of the radially blocked annulus was measured in an identical manner to the open case discussed in the previous chapter. These heat transport measurements were compared to the theoretical prediction made by Rayer et al. [1998] for a geostrophic overturning cell:

$$H = \frac{\rho_0 c g \alpha \Delta T_B \Delta T_z d^2}{24\Omega}, \quad (5.3)$$

where here ΔT_z is the temperature drop from lid to base, and ΔT_B is the temperature drop across the radial barrier. ΔT_z was found to be $\sim 3/4 (T_B - T_A)$ for the $\kappa = 1.3 \times 10^{-3}$ cm² / s fluid. This contrasts with the $\Delta T_z \sim 1/2 (T_B - T_A)$ for a similar fluid in an open tank geometry [Rayer et al., 1998]. This prediction is compared with the measured advective heat transport in figure 5.5. For the Prandtl number 14 fluid the η circulation mechanism gives reasonably good agreement with the measured system advective heat transport, particularly for $\Omega > \sim 3.0$ rad / s. In contrast to this, for the Prandtl number 3.5 fluid there is a relatively poor agreement, with the heat transport at $\Omega = 4$ rad / s and

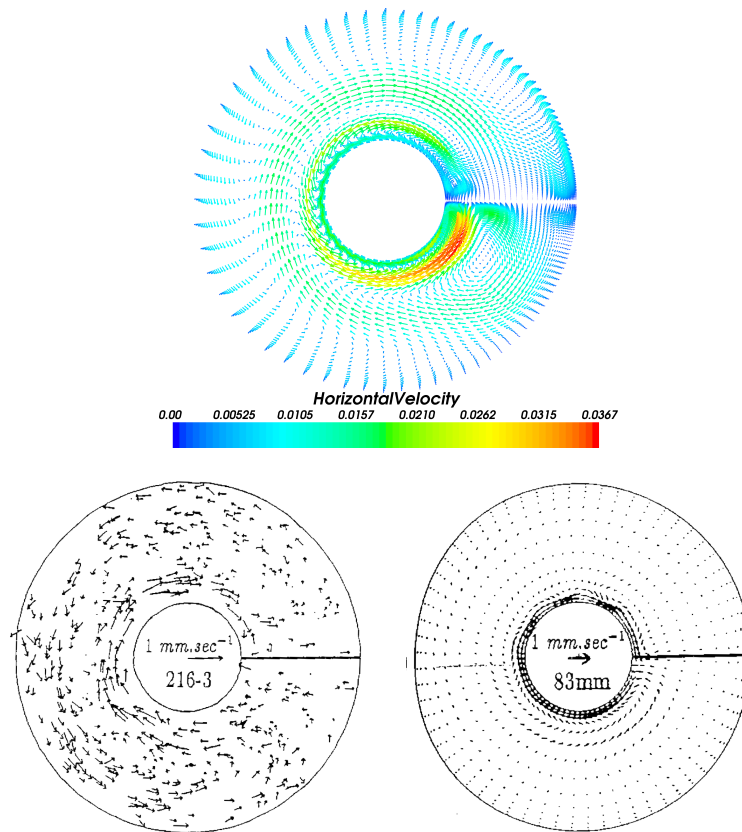


Figure 5.2: Above: ICOM simulation of the thermally driven annulus with full insulating radial barrier for a Prandtl number 14 fluid at $\Omega = 1$ rad / s, viewed at mid-height. Lower left: Comparable laboratory observation at $\Omega = 1.176$ rad / s, viewed at mid-height (from Rayer [1992] figure 5.2c). Lower right: Simulation using a modified version of the Farnell and Plumb [1975, 1976] annulus model, at $\Omega = 1.2$ rad / s, viewed 8.3 cm from tank base (from Rayer [1992] figure 5.1c).

above being inadequately explained by the meridional overturning transport mechanism.

One can make a “conservation of isotherms” argument, stating that the temperature drop across the radial barrier necessary to maintain the system heat transport at its non-rotating value cannot exceed the temperature forcing. Measurements of $\Delta \bar{T}_B / (T_B - T_A)$ are shown in figure 5.6. It can be seen that for the Prandtl number 14 fluid the temperature drop across the radial barrier fails to reach saturation. Hence an increase in rotation rate can, for the range of experiments conducted, always be compensated for by a corresponding azimuthal temperature gradient. In contrast to this, for the Prandtl number 3.5 fluid there is a saturation of the barrier temperature drop, followed by a small mean

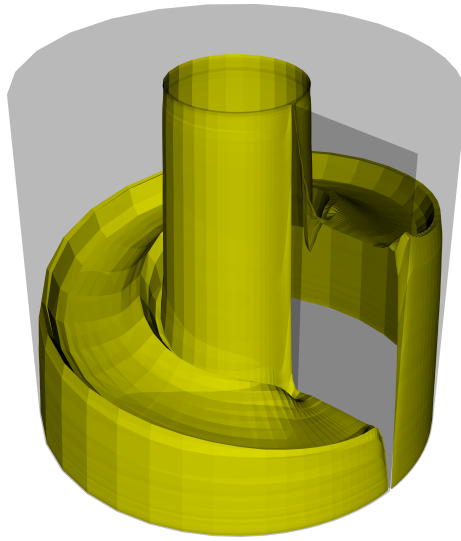


Figure 5.3: $T = 3/4(T_B - T_A)$ isotherm for an ICOM simulation of the thermally driven annulus with full insulating radial barrier for a Prandtl number 14 fluid at $\Omega = 1$ rad / s, demonstrating the temperature drop across the radial barrier.

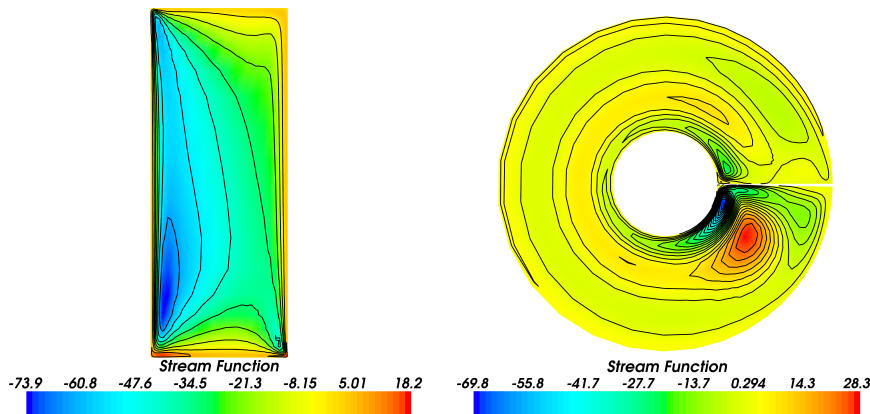


Figure 5.4: Left: Overturning streamfunction for an ICOM simulation of the thermally driven annulus with full insulating radial barrier for a Prandtl number 14 fluid at $\Omega = 1$ rad / s (10 contours shown). A single dominant overturning cell is evident. Right: Barotropic streamfunction for this same simulation (25 contours shown). Note the sign change in the streamfunction towards the tank inner wall, indicating a reversal in flow direction. This barotropic shear is associated with small scale eddies in this region. Stream function units are cm^2 / s .

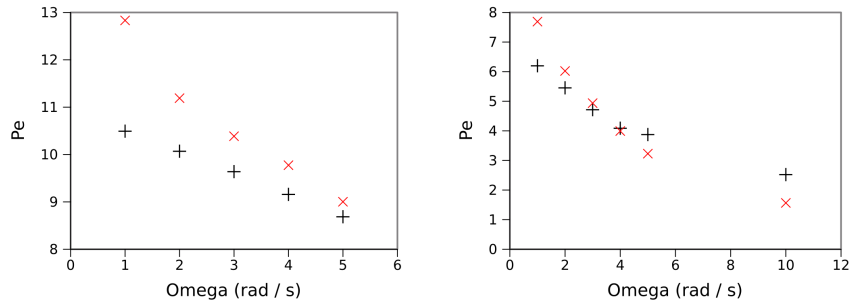


Figure 5.5: Heat transport measurements (in black) for the thermally driven annulus with full insulating radial barrier for the Prandtl number 14 fluid (left) and Prandtl number 3.5 fluid (right). Shown in red are predictions of the heat transport based upon the presence of a geostrophic overturning cell.

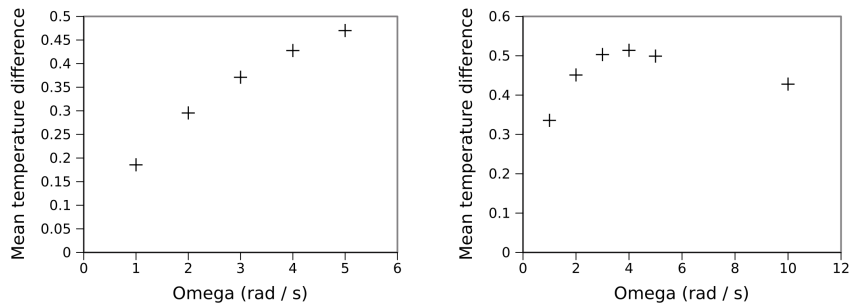


Figure 5.6: Measurements of the mean temperature drop, $\Delta\bar{T}_B/(T_B - T_A)$, across the radial barrier in ICOM simulations of the thermally driven annulus with full radial barrier, for Prandtl number 14 (left) and 3.5 (right).

decrease. These observations agree with the discussion in Rayer et al. [1998]. However, for the Prandtl number 3.5 fluid the expected monotonicity is not observed, indicating the presence of complicating processes influencing the radial barrier temperature drop. The saturation of the azimuthal temperature gradient indicates that, for these simulations, an increase in rotation rate cannot be compensated for by any corresponding azimuthal temperature gradient.

Hence it can be deduced that initially the heat transport of the radial barrier annulus is maintained by a temperature drop across the radial barrier leading to an azimuthal temperature gradient sufficient to maintain meridional overturning as in the non-rotating (natural convection) case. For increased rotation rate, conservation of isotherms means that this compensating effect can no longer be maintained. The decrease in magnitude of the η circulation is associated with the generation of eddies. This suggests that, at increased rotation rate, the

heat transport of the system is instead maintained through the generation of baroclinic eddies. These conclusions are consistent with the previous laboratory work of Rayer [1992] and Rayer et al. [1998]

5.4 Summary

Numerical simulations of the radial barrier annulus have been conducted with the Imperial College Ocean Model. The simulations are observed to give reasonable qualitative agreement with laboratory experiments, albeit with some deviations at the tank inner wall. Discrepancies between the horizontal flow observed in the numerical simulations and the laboratory experiments are attributed to numerical error or due to the presence of in-situ thermocouples in experiment. These simulations have been used for direct observation of the geostrophic overturning transport mechanism, and to make observations of the corresponding temperature drop across the radial barrier. They have further been used for numerical assessment of the mechanisms via which the influence of rotation is filtered from certain global features in the move from a multiply connected to simply connected topology.

Remaining work to be conducted for these experiments includes: direct quantitative comparison of the heat transport and temperature profiles of the system against laboratory data, investigations into the introduction of sloping topography and the corresponding promotion or suppression of the eddies observed at high thermal Rossby number, and investigation into higher Taylor number experiments using dynamic mesh adaptivity to resolve the multi-scale flows.

Chapter 6

Summary and Future Work

6.1 Future Work

The emphasis of remaining research to be conducted in this DPhil project will be on the extension of simulations of annulus configurations that have previously been challenging to simulate numerically. In chapter 5 it was shown that ICOM simulations of the standard open tank annulus could be extended to simulations of the annulus with a full radial barrier, and that unstructured mesh diagnostics could be used to give an insight into the physics of the system.

Very recently, simulations in high Taylor number flows have been conducted using ICOM in full mesh-adaptive mode. An example is shown in figure 6.1. There is a striking similarity between the numerical simulation and the laboratory reference. Attempts were made to simulate this configuration using static meshes, as used in chapter 5. However, all attempts using the $24 \times 24 \times 64$ Farnell and Plumb [1975, 1976] mesh were unsuccessful, even when using advective upwinding schemes. Only dynamic mesh adaptive simulations or high resolution static simulations were found to be numerically stable. This indicates that, while there are possible issues with mesh adaptivity as discussed in chapter 4, dynamic mesh adaptivity may enable simulations of flow regimes that are unachievable by other methods without very significant investment of computational resources.

The key areas to be focused on in remaining research are:

1. Completion of model validation;
2. Simulations of the rotating annulus with sloping lid / base topography;
3. Simulations of the rotating annulus at high Taylor number.

Concerning point 1, additional laboratory data for the heat flow annulus (open

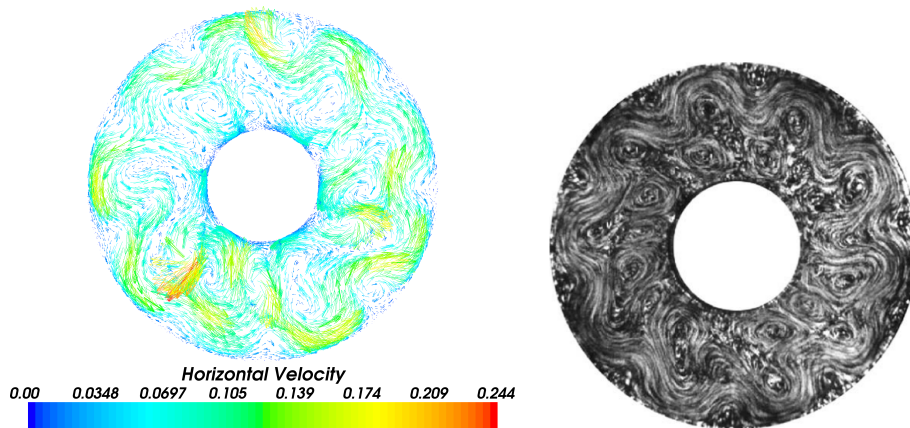


Figure 6.1: Left: Adaptive mesh ICOM simulation of a high Taylor number thermally driven annulus simulation with 22° sloping top and bottom topography (shallow at tank centre), with Taylor number 0.097 and thermal Rossby number 6×10^7 . Other simulation parameters are as described in Wordsworth et al. [2008]. Right: Streak image of a comparable laboratory experiment (from Wordsworth et al. [2008] figure 3a).

and blocked) has been extracted from the annulus data archives and is currently undergoing processing. In particular, in-situ thermocouple measurements will allow direct quantitative comparison of the magnitude of wave modes, at least for the temperature field at mid radius. This, when combined with measurements of the system heat transport, will enable more concrete conclusions to be made concerning the influence of dynamic mesh adaptivity on rotating annulus simulations.

For point 2, emphasis will be on the comparison of eddy growth with theory, including zero potential vorticity formulations and internal jet formulations. Some preliminary simulations of rotating periodic channel flows with topography have already been conducted. These simulations could be extended to the introduction of sloping topography into standard and blocked annulus geometries, in the latter case enabling a study of the suppression or promotion of internal eddies by topography.

Finally, for point 3, further analysis of the high Taylor number flows (as in figure 6.1) will enable more detailed quantitative study of the physics of banded zonal jet formation, and the testing of recent suggestions concerning the locality (in Fourier space) of eddy energy transfer [Wordsworth, 2008, Wordsworth et al., 2008].

6.2 Timeline for Completion

Sept 2009 - Dec 2009	<p>High resolution open geometry simulations</p> <p>Processing of laboratory data archive and extraction of further data for comparison</p> <p>Completion of standard open geometry validation</p> <p>High Taylor number open / topographic simulations</p> <p>Investigation of internal banded zonal jet formation mechanisms</p>
Jan 2010 - Feb 2010	<p>Sloping bottom topography simulations</p> <p>Comparison of topographic simulations with theories for eddy growth</p>
Mar 2010 - Apr 2010	<p>End of thesis simulations</p> <p>Completion of remaining simulation data analysis</p>
May 2010 onwards	Write thesis

6.3 Summary

The rotating annulus is a classic experiment containing key aspects of the physics of a geophysical fluid while removing certain complicating factors. A simplified annulus system is able to capture some of the physics of the larger scale flows, but in a controlled, reproducible manner and with chosen system parameters. There is a wealth of existing laboratory data available concerning the system.

The Imperial College Ocean Model, being implemented as part of the general computational fluid dynamics framework Fluidity, is an in-development ocean model implementing new technologies that have particular applicability to simulations of the annulus. The use of an unstructured mesh makes simulations of non-coordinate-conforming geometries possible without special considerations, while the use of mesh adaptivity techniques allows multi-scale flows to be investigated at reduced computational cost. Techniques for accurate representation of balance ensure that the solutions are physically reasonable even on arbitrarily unstructured meshes.

Simulations of the standard thermally driven annulus have been conducted and compared quantitatively with experiment. It was found that, in static mesh mode, the model was able to give a credible representation of the system heat transport. It was further found that the introduction of dynamic mesh adaptiv-

ity led to a systematic reduction in the measured system heat transport. This reduction is attributed to either the influence of mesh-to-mesh projections, or an offset between the converged model solution and the laboratory experiment. High resolution static mesh simulations will enable this to be further investigated.

Simulations of the thermally driven annulus were extended to enable simulations with a full radial barrier present. It was found that the simulation heat transport could be explained by a geostrophic overturning cell, and that the breakdown of this as a transport mechanism was associated with the appearance of internal, possibly baroclinic, eddies. New simulations extending these simulations to higher rotation rates in open geometries are under way, and have a qualitatively favourable comparison with experiment.

At the end of the second year, quantitative validation has shown that the model is able to give a reasonable representation of real world annulus flows. It has further been shown that there are potential pitfalls with the introduction of dynamic mesh adaptivity. However, physically interesting flows (particularly at high Taylor number) have been found to be inaccessible without the use of dynamic mesh adaptivity (at least at reasonable computational cost). At the end of the second year, this project is now in a position to conduct investigations into annulus configurations that have previously proven challenging to simulate numerically. These include studies into the physics of baroclinic instability theory in the presence of sloping topography, and the physics of banded zonal jet formation.

Appendix A

Equations of Fluid Flow

In this section the following symbols are used:

$D_t = \partial/\partial t + u \cdot \nabla$	Material derivative
u	Eulerian velocity
Ω	Rotation vector
p	Pressure
g	Gravity
ν	Kinematic viscosity (tensor)
$\rho' = \rho/\rho_0$	Perturbation density
ρ	Density relative to the reference density
ρ_0	Reference density ($ \rho - \rho_0 \ll 1$)
T	Temperature relative to the reference temperature
T_0	Reference temperature ($ T - T_0 \ll 1$)
κ	Diffusivity (tensor)
α	Thermal expansion coefficient

Fluidity can solve very general equations of fluid flow, including multiphase simulations, mixed solid-fluid simulations and incompressible flows. However, the standard equations solved for a geophysical problem (an “ICOM mode” simulation) are listed below. See Ford et al. [2004a] and Piggott et al. [2008] for further details.

Momentum Equation

The Navier-Stokes equation in a rotating frame under the Boussinesq (neglecting density variation except where coupled with gravity) and traditional (neglecting horizontal components of the Coriolis force) approximations, neglecting the centrifugal force and for an incompressible Newtonian fluid:

$$D_t u + 2\Omega \times u = -\nabla p + \rho' g + \nabla \cdot (\nu \nabla u). \quad (\text{A.1})$$

Continuity Equation

The continuity (mass conservation) equation for an incompressible fluid:

$$\nabla \cdot \mathbf{u} = 0. \tag{A.2}$$

Temperature Equation

The heat transport equation:

$$D_t T = \nabla \cdot (\kappa \nabla T). \tag{A.3}$$

Equation of State

The equation of state for a linear fluid:

$$\rho' = -\alpha(T - T_0). \tag{A.4}$$

Appendix B

Dimensionless Parameters

In this section the following symbols are used:

a	Smaller annulus radius
b	Larger annulus radius
d	Annulus height
α	Thermal expansion coefficient
κ	Diffusivity
ν	Kinematic viscosity
g	Gravity
T_A	Inner side-wall temperature
T_B	Outer side-wall temperature

For a standard annulus as in figure 2.2 with a linear equation of state and under the Boussinesq approximation, one set of non-dimensional parameters for the system is:

Vertical to horizontal aspect ratio

$$A_d = \frac{b - a}{d} \quad (\text{B.1})$$

Typical annulus magnitude ~ 1 .

Radii aspect ratio

$$A_r = \frac{b}{a} \quad (\text{B.2})$$

Typical annulus magnitude ~ 1 .

Prandtl number

$$Pr = \frac{\nu}{\kappa} \quad (\text{B.3})$$

Expresses the strength of viscosity relative to thermal diffusion. Typical annulus magnitude ~ 10 .

Thermal Rossby number

$$\Theta = \frac{g\alpha(T_B - T_A)}{\Omega^2} \frac{d}{(b-a)^2} \quad (\text{B.4})$$

Expresses the strength of buoyancy relative to rotation [Hide and Mason, 1975]. Typical annulus magnitude ~ 1 .

Taylor number

$$T = \frac{\Omega^2}{\nu^2} \frac{4(b-a)^5}{d} \quad (\text{B.5})$$

Expresses the strength of rotation relative to viscosity [Hide and Mason, 1975]. Typical annulus magnitude $\sim 10^6$.

Rayleigh number

$$Ra = \frac{g\alpha(T_B - T_A)(b-a)^3}{\nu\kappa} \quad (\text{B.6})$$

A parameter defining the nature of convection. For natural convection, the system heat transport is a function only of the Rayleigh number and the Prandtl number [Landau and Lifshitz, 1959]. Typical annulus magnitude $\sim 10^6$.

Bibliography

- F. Alauzet, A. Loseille, A. Dervieux, and P. Frey. Multi-dimensional continuous metric for mesh adaptation. In *Proc. 15th Int. Meshing Roundtable*, pages 191–214, 2006.
- M. Bader, S. Schraufstetter, C. A. Vigh, and J. Behrens. Memory efficient adaptive mesh generation and implementation of multigrid algorithms using Sierpinski curves. *International Journal of Computational Science and Engineering*, 4(1):12–21, 2008.
- M. Bajo, G. Umgiesser, and A. Borghesan. Storm surge forecasting in venice with a combination of hydrodynamic modelling and neural networks. In *EGU General Assembly*, volume 10, April 2008.
- V. Barcilon. Role of the Ekman layers in the stability of the symmetric regime obtained in a rotating annulus. *Journal of the Atmospheric Sciences*, 21(3): 291–299, 1964.
- G. K. Batchelor. *An introduction to fluid mechanics*. Cambridge University Press Cambridge, 1967.
- M. J. Bell and A. A. White. The Stability of Internal Baroclinic Jets: Some Analytical Results. *Journal of the Atmospheric Sciences*, 45(18):2571–2590, 1988.
- FP Bretherton. Critical layer instability in baroclinic flows. *Quarterly Journal of the Royal Meteorological Society*, 92(393), 1966.
- A. N. Brooks and T. J. R. Hughes. Streamline upwind/Petrov-Galerkin formulations for convection dominated flows with particular emphasis on the incompressible Navier-Stokes equations. *Comput. Methods Appl. Mech. Eng.*, 32:199–259, 1982.
- J. G. Charney. The dynamics of long waves in a baroclinic westerly current. *Journal of the Atmospheric Sciences*, 4(5):136–162, 1947.
- C. Chen, H. Huang, R. C. Beardsley, H. Liu, Q. Xu, and G. Cowles. A finite volume numerical approach for coastal ocean circulation studies: comparisons with finite difference models. *J. Geophys. Res.*, 112:C03018, 2007.
- R. Comblen, S. Legrand, E. Deleersnijder, and V. Legat. A finite element method for solving the shallow water equations on the sphere. *Ocean Modelling*, 28(1-3):12–23, 2009.

- C. J. Cotter. A family of mixed finite element pairs with optimal geostrophic balance. *Arxiv preprint arXiv:0905.0126*, 2009a.
- C. J. Cotter, D. A. Ham, and C. C. Pain. A mixed discontinuous/continuous finite element pair for shallow-water ocean modelling. *Ocean Modelling*, 26(1-2):86–90, 2009a.
- C. J. Cotter, D. A. Ham, C. C. Pain, and S. Reich. LBB stability of a mixed Galerkin finite element pair for fluid flow simulations. *Journal of Computational Physics*, 228(2):336–348, 2009b.
- Colin Cotter. Finite element methods that perfectly preserve geostrophic balances. Waveflow meeting, May 2009b.
- R. Courant, K. Friedrichs, and H. Lewy. Ueber die partiellen differenzgleichungen der mathematischen physik. *Mathematische Annalen*, 100(100):32–74, 1928.
- G. de Vahl Davis and I. P. Jones. Natural convection of air in a square cavity: a bench mark numerical solution. *International Journal for Numerical Methods in Fluids*, 3(3), 1983.
- Jean Donea and Antonio Huerta. *Finite Element Methods for Flow Problems*. John Wiley and Sons Ltd, 2003.
- E. T. Eady. Long waves and cyclone waves. *Tellus*, 1(3):33–52, 1949.
- S. S. Elliott. *Numerical studies of baroclinic instability*. PhD thesis, University of Oxford, 1995.
- L. Farnell and R. A. Plumb. Numerical integration of flow in a rotating annulus i: axisymmetric model. Occasional Note Met O 21 75/3, Geophysical Fluid Dynamics Laboratory, Meteorological Office, Bracknell, Berkshire., December 1975.
- L. Farnell and R. A. Plumb. Numerical integration of flow in a rotating annulus ii: three dimensional model. Occasional Note Met O 21 76/1, Geophysical Fluid Dynamics Laboratory, Meteorological Office, Bracknell, Berkshire., February 1976.
- P. E. Farrell, M. D. Piggott, and G. J. Gorman. Automated continuous code verification and the imperial college ocean model. Seventh International Workshop on Unstructured Grid Numerical Modelling of Coastal, Shelf and Ocean Flows, 2008.
- P. E. Farrell, M. D. Piggott, C. C. Pain, G. J. Gorman, and C. R. Wilson. Conservative interpolation between unstructured meshes via supermesh construction. *Computer Methods in Applied Mechanics and Engineering*, 198(33-36):2632–2642, 2009.
- Patrick Farrell. Error measurement and adaptive strategies. Seminar, 16 May 2008.

- R. Ford, C. C. Pain, M. D. Piggott, A. J. H. Goddard, C. R. E. de Oliveira, and A. P. Umpleby. A nonhydrostatic finite-element model for three-dimensional stratified oceanic flows. Part I: Model Formulation. *Monthly Weather Review*, 132(12):2816–2831, 2004a.
- R. Ford, C. C. Pain, M. D. Piggott, A. J. H. Goddard, C. R. E. de Oliveira, and A. P. Umpleby. A nonhydrostatic finite-element model for three-dimensional stratified oceanic flows. Part II: Model validation. *Monthly weather review*, 132(12):2832–2844, 2004b.
- W. W. Fowlis and R. Hide. Thermal convection in a rotating annulus of liquid: effect of viscosity on the transition between axisymmetric and non-axisymmetric flow regimes. *Journal of the Atmospheric Sciences*, 22(5):541–558, 1965.
- W. G. Fruh and P. L. Read. Wave interactions and the transition to chaos of baroclinic waves in a thermally driven rotating annulus. *Philosophical Transactions-Mathematical Physical and Engineering Sciences*, 355(1722):101–154, 1997.
- D. Fultz. Experimental analogies to atmospheric motions. *Compendium of meteorology*, pages 1235–1248, 1951.
- D. Fultz, R. R. Long, G. V. Owens, W. Bohan, R. Kaylor, and J. Weil. Studies of thermal convection in a rotating cylinder with some implications for large-scale atmospheric motions. 1959.
- J. E. Geisler, E. J. Pitcher, and R. C. Malone. Rotating-fluid experiments with an atmospheric general circulation model. *Journal of Geophysical Research*, 88(C14):9706–9716, 1983.
- A. E. Gill. The boundary-layer regime for convection in a rectangular cavity. *Journal of Fluid Mechanics*, 26:515–536, 1966.
- JSA Green, BJ Hoskins, ME McIntyre, and AW Robertson. Comments 'On the Use and Significance of Isentropic Potential Vorticity Maps' By BJ Hoskins, ME McIntyre and AW Robertson (October 1985, 111, 877-946). *Quarterly Journal of the Royal Meteorological Society*, 113(475), 1987.
- S. M. Griffies, C. Boning, F. O. Bryan, E. P. Chassignet, R. Gerdes, H. Hasumi, A. Hirst, A. M. Treguier, and D. Webb. Developments in ocean climate modelling. *Ocean Modelling*, 2(3/4):123–192, 2000.
- D. A. Ham, P. E. Farrell, G. J. Gorman, J. R. Maddison, C. R. Wilson, S. C. Kramer, J. Shipton, G. S. Collins, C. J. Cotter, and M. D. Piggott. Spud 1.0: generalising and automating the user interfaces of scientific computer models. *Geoscientific Model Development*, 2:33–42, 2008.
- R. L. Haney. On the pressure gradient force over steep topography in sigma coordinate ocean models. *Journal of Physical Oceanography*, 21(4):610–619, 1991.
- R. Hide. Some experiments on thermal convection in a rotating liquid. *Quarterly Journal of the Royal Meteorological Society*, 79(339), 1953.

- R. Hide. On source-sink flows in a rotating fluid. *Journal of Fluid Mechanics*, 32, 1968.
- R. Hide. *Some laboratory experiments on free thermal convection in a rotating fluid subject to a horizontal temperature gradient and their relation to the theory of the global atmospheric circulation*, pages 196–221. London: Royal Meteorological Society, 1969.
- R. Hide. On the effects of rotation on fluid motions in cylindrical containers of various shapes and topological characteristics. *Dynamics of Atmospheres and Oceans*, 27(1-4):243–256, 1997.
- R. Hide and P. J. Mason. Baroclinic waves in a rotating fluid subject to internal heating. *Philosophical Transactions for the Royal Society of London. Series A, Mathematical and Physical Sciences*, pages 201–232, 1970.
- R. Hide and P. J. Mason. Sloping convection in a rotating fluid. *Advances in Physics*, 24(1):47–100, 1975.
- Raymond Hide. Geomagnetism, “vacillation”, atmospheric predicability and “deterministic chaos”. *Pontifical Academy of Sciences Acta*, 18:257–254, 2006.
- B. P. Hignett, A. A. White, R. D. Carter, W. D. N. Jackson, and R. M. Small. A comparison of laboratory measurements and numerical simulations of baroclinic wave flows in a rotating cylindrical annulus. *Quarterly Journal of the Royal Meteorological Society*, 111(463), 1985.
- T. Hughes. Recent progress in the development and understanding of SUPG methods with special reference to the compressible Euler and Navier-Stokes equations (Streamline-Upwind/Petrov-Galerkin). *International Journal for Numerical Methods in Fluids*, 7:1261–1275, 1987.
- I. N. James, P. R. Jonas, and L. Farnell. A combined laboratory and numerical study of fully developed steady baroclinic waves in a cylindrical annulus. *Quarterly Journal of the Royal Meteorological Society*, 107(451), 1981.
- O. A. Ladyzhenskaya. The mathematical theory of viscous incompressible flow. *New York*, page 10, 1969.
- L D Landau and E M Lifshitz. *Fluid Mechanics*, volume 6 of *Course of Theoretical Physics*. Butterworth-Heinemann, 2 edition, 1959.
- BP Leonard. The ULTIMATE conservative difference scheme applied to unsteady one-dimensional advection. *Computer methods in applied mechanics and engineering*, 88(1):17–74, 1991.
- Edward N. Lorenz. *The Nature and Theory of the General Circulation of the Atmosphere*. World Meteorological Organisation, 1967.
- E.N. Lorenz. Deterministic nonperiodic flow. *Journal of the atmospheric sciences*, 20(2):130–141, 1963.
- P. J. Mason. Baroclinic waves in a container with sloping end walls. *Philosophical Transactions for the Royal Society of London. Series A, Mathematical and Physical Sciences*, 278(1284):397–445, 1975.

- S. Micheletti and S. Perotto. Reliability and efficiency of an anisotropic Zienkiewicz–Zhu error estimator. *Computer Methods in Applied Mechanics and Engineering*, 195(9-12):799–835, 2006.
- MORALS. The met office / oxford rotating annulus simulation. Source code. Version 081003.
- NASA/JPL. South polar projection of earth. <http://photojournal.jpl.nasa.gov/catalog/PIA00729>.
- C. C. Pain, A. P. Umpleby, C. R. E. De Oliveira, and A. J. H. Goddard. Tetrahedral mesh optimisation and adaptivity for steady-state and transient finite element calculations. *Computer Methods in Applied Mechanics and Engineering*, 190(29-30):3771–3796, 2001.
- C. C. Pain, M. D. Piggott, A. J. H. Goddard, F. Fang, G. J. Gorman, D. P. Marshall, M. D. Eaton, P. W. Power, and C. R. E. de Oliveira. Three-dimensional unstructured mesh ocean modelling. *Ocean Modelling*, 10(1-2):5–33, 2005.
- M. D. Piggott, C. C. Pain, G. J. Gorman, P. W. Power, and A. J. H. Goddard. h, r, and hr adaptivity with applications in numerical ocean modelling. *Ocean Modelling*, 10(1-2):95–113, 2006.
- M. D. Piggott, G. J. Gorman, C. C. Pain, P. A. Allison, A. S. Candy, B. T. Martin, and M. R. Wells. A new computational framework for multi-scale ocean modelling based on adapting unstructured meshes. *International Journal for Numerical Methods in Fluids*, 56(8):1003, 2008.
- P. W. Power, M. D. Piggott, F. Fang, G. J. Gorman, C. C. Pain, D. P. Marshall, A. J. H. Goddard, and I. M. Navon. Adjoint goal-based error norms for adaptive mesh ocean modelling. *Ocean Modelling*, 15(1-2):3–38, 2006.
- Q. G. Rayer. *An experimental investigation of heat transfer by large scale motions in rotating fluids*. PhD thesis, University of Oxford, 1992.
- Q. G. Rayer. A Numerical Investigation of the Flow in a Fully Blocked Differentially Heated Rotating Fluid Annulus. *International Journal of Modern Physics C-Physics and Computer*, 5(2):25–28, 1994.
- Q. G. Rayer, D. W. Johnson, and R. Hide. Thermal convection in a rotating fluid annulus blocked by a radial barrier. *Geophysical & Astrophysical Fluid Dynamics*, 87(3):215–252, 1998.
- W. H. Raymond and A. Garder. Selective damping in a Galerkin method for solving wave problems with variable grids. *Monthly weather review*, 104(12):1583–1590, 1976.
- P. L. Read. *Rotating Annulus Flows And Baroclinic Waves*, chapter IV.3, pages 185–214. Springer-Verlag, Wien, 1992.
- P.L. Read. A combined laboratory and numerical study of heat transport by baroclinic eddies and axisymmetric flows. *Journal of Fluid Mechanics*, 489:301–323, 2003.

- S. H. Risch. *Large-scale interactions in baroclinic flow with topography*. PhD thesis, University of Oxford, 1999.
- P. J. Roache. Code verification by the method of manufactured solutions. *Journal of Fluids Engineering*, 124:4, 2002.
- K. Salari and P. Knupp. Code verification by the method of manufactured solutions. *Sandia National Labs., SAND2000-1444, Albuquerque, NM*, 2000.
- Spencer Sherwin. Discontinuous galerkin methods using spectral/hp element discretisations: Why and when is it useful to apply dg. One-Day Workshop on the Discontinuous Galerkin Method and It's Applications, 31st October 2007. University of Reading.
- B. Sitte and C. Egbers. Higher order dynamics of baroclinic waves. In *Physics of Rotating Fluids (Proc. 11th Int. Couette-Taylor Workshop, 20-23 July 1999, Bremen, Germany)*, edited by: Pfister, G. and Egbers, C, volume 549. Springer, 2000.
- Gilbert Strang. *Linear Algebra and its Applications*. Thomson Learning, Inc., 3 edition, 1988.
- P. K. Sweby. High resolution schemes using flux limiters for hyperbolic conservation laws. *SIAM J. Numer. Anal.*, 21(5):995–1011, 1984.
- G. I. Taylor. Motion of solids in fluids when the flow is not irrotational. *Proceedings of the Royal Society of London. Series A, Containing Papers of a Mathematical and Physical Character*, pages 99–113, 1917.
- Y. Tong, S. Lombeyda, A. N. Hirani, and M. Desbrun. Discrete multiscale vector field decomposition. *ACM Transactions on Graphics*, 22(3):445–452, 2003.
- G. K. Vallis. *Atmospheric and oceanic fluid dynamics: fundamentals and large-scale circulation*. Cambridge University Press, 2006.
- F. Vettin. Ueber den aufsteigenden Luftstrom, die Entstehung des Hagels und der Wirbel-Stürme. *Annalen der Physik*, 178(10):246–255, 1857.
- A. A. White. The dynamics of rotating fluids: Numerical modelling of annulus flows. *Meteorological Magazine*, 117(1387):54–63, 1988.
- A. Wiebel, G. Scheuermann, and C. Garth. *Feature detection in vector fields using the helmholtz-hodge decomposition*. PhD thesis, Masters thesis, University of Kaiserslautern, 2004.
- G. P. Williams. Numerical integration of the three-dimensional Navier-Stokes equations for incompressible flow. *Journal of Fluid Mechanics*, 37:727–750, 1969.
- P. D. Williams, T. W. N. Haine, P. L. Read, S. R. Lewis, and Y. H. Yamazaki. QUAGMIRE v1. 3: a quasi-geostrophic model for investigating rotating fluids experiments. *Geoscientific Model Development*, 2:13–32, 2009.

- R. D. Wordsworth. *Theoretical and experimental investigations of turbulent jet formation in planetary fluid dynamics*. PhD thesis, University of Oxford, 2008.
- R. D. Wordsworth, P. L. Read, and Y. H. Yamazaki. Turbulence, waves, and jets in a differentially heated rotating annulus experiment. *Physics of Fluids*, 20:126602, 2008.
- J. Z. Wu, H. Y. Ma, and M. D. Zhou. *Vorticity and vortex dynamics*. Springer, 2006.
- R. M. B. Young and P. L. Read. Flow transitions resembling bifurcations of the logistic map in simulations of the baroclinic rotating annulus. *Physica D: Nonlinear Phenomena*, 237(18):2251–2262, 2008a.
- R. M. B. Young and P. L. Read. Breeding and predictability in the baroclinic rotating annulus using a perfect model. *Nonlinear Processes in Geophysics*, 15(3):469–487, 2008b.
- O. C. Zienkiewicz and R. L. Taylor. *The Finite Element Method Volume 3 - Fluid Mechanics*, volume 3. Butterworth-Heinemann, 5 edition, 2000.
- O. C. Zienkiewicz and J. Z. Zhu. Adaptivity and mesh generation. *International Journal for Numerical Methods in Engineering*, 32(4), 1991.